minerals

MDPI

Article

Multiple Sulfur Isotope Evidence for Bacterial Sulfate Reduction and Sulfate Disproportionation Operated in Mesoarchaean Rocks of the Karelian Craton

Sergey V. Vysotskiy [1], Tatyana A. Velivetskaya [1,*], Aleksandr V. Ignatiev [1], Aleksandr I. Slabunov [2] and Anna V. Aseeva [1]

[1] Far East Geological Institute, Far Eastern Branch of the Russian Academy of Sciences, 690022 Vladivostok, Russia
[2] Karelian Research Center, Institute of Geology, Russian Academy of Sciences, 185910 Petrozavodsk, Russia
* Correspondence: velivetskaya@mail.ru

Abstract: Sulfur isotope in sulfides from the Paleoarchean and the Neoarchean sedimentary rocks evidence microbial sulfur metabolism in Archean sulfur cycle. However, sulfur metabolism for the Mesoarchean interval is less obvious since evidence for a large range in sulfur isotope values has not yet been observed in Mesoarchean samples. We report the results of multiple sulfur isotope measurements for sulfide minerals from ~2.8 Ga sedimentary rocks in the southeastern part of the Karelian Craton. In situ isotope analysis of sulfide grains have been performed using a femtosecond laser-ablation fluorination method. Sulfide samples studied here yielded $\Delta^{33}S$ values between −0.3 and +2.7‰ and $\delta^{34}S$ values between −10 and +33‰. The $\Delta^{33}S$ dataset was interpreted to indicate the incorporation of sulfur from two coexisting sulfur pools, photolytic sulfate and photolytically derived elemental sulfur. We suggest that the relative contributions of these $\Delta^{33}S$ different pools to the pyritic sulfur could be controlled by the metabolic activity of coexisting sulfate-reducing and sulfur-disproportionating bacteria during pyrite formation. We therefore suggest the operation of different metabolic pathways of sulfur in Mesoarchean sedimentary environments.

Keywords: Mesoarchean; multiple sulfur isotopes; bacterial sulfate reduction; sulfur disproportionation

check for updates

Citation: Vysotskiy, S.V.; Velivetskaya, T.A.; Ignatiev, A.V.; Slabunov, A.I.; Aseeva, A.V. Multiple Sulfur Isotope Evidence for Bacterial Sulfate Reduction and Sulfate Disproportionation Operated in Mesoarchaean Rocks of the Karelian Craton. *Minerals* **2022**, *12*, 1143. https://doi.org/10.3390/min12091143

Academic Editor: José Javier Alvaro

Received: 1 July 2022
Accepted: 7 September 2022
Published: 9 September 2022

Publisher's Note: MDPI stays neutral with regard to jurisdictional claims in published maps and institutional affiliations.

Copyright: © 2022 by the authors. Licensee MDPI, Basel, Switzerland. This article is an open access article distributed under the terms and conditions of the Creative Commons Attribution (CC BY) license (https://creativecommons.org/licenses/by/4.0/).

1. Introduction

Bacteria are widespread prokaryotic organisms observed in different modern environments [1,2] and are thought to have already inhabited the Earth in the Paleoarchean [3]. Microbial activity in Paleoarchean (3.6–3.2 Ga) sedimentary environments has been identified on the basis of a combination of mass-dependent and mass-independent fractionation of sulfur isotopes ($\delta^{34}S$ and $\Delta^{33}S$ values) in sulfides from the Dresser Formation (3.49 Ga) in the Pilbara Craton, Western Australia [4–9] and from the Barberton Greenstone Belt, South Africa [5,10–12]. The strongly negative $\delta^{34}S$ values recorded in sulfides from ancient sediments have been considered as one of the principal arguments for a biological genesis of sulfides [13,14], whereas reactions of thermochemical sulfate reduction have been proposed as an alternative for the process of pyrite formation with negative $\delta^{34}S$ values in the Dresser Formation [15].

Studies of sulfide minerals from Neoarchean (2.8–2.5 Ga) rocks of Western Australia, South Africa and Brazil [16–21] have also shown large sulfur isotope fractionations (collectively, $\delta^{34}S$ data published in these studies range from values of approximately −30‰ to +20‰), that supports the existence of microbial life during the Neoarchean.

In contrast to the relatively wide range of variability for $\delta^{34}S$ values in Paleoarchean and Neoarchean sediments, sulfur isotope data that are currently available in the literature for Mesoarchean (3.2–2.8 Ga) sediments have shown a significantly smaller range in $\delta^{34}S$ values. For example, Mesoarchean samples from southern Africa and Western Australia yielded $\delta^{34}S$ values that predominantly grouped within a range from −3‰ to +7‰ [22–24]. Based on

the lack of significant fractionations in ^{34}S that is expected in microbially driven processes, Ono and coauthors [24] considered microbial sulfur cycling to be a minor factor for the transfer of sulfur species from the oceanic reservoir into sulfide sulfur in sedimentary rocks of the ~2.9 Ga Mozaan Group of the Pongola Supergroup in Southern Africa. The lack of evidence for large sulfur isotope fractionations has been linked to the limited bacterial sulfur cycling in ancient pyrite-forming environments [25]. However, despite the smaller $\delta^{34}S$ variations in Mesoarchean compared to other Archaean intervals, there is still uncertainty with regard to the presence of microorganisms in Mesoarchean oceans since a narrow range in $\delta^{34}S$ values in sulfides does not yet indicate the absence of biogenic transformations of sulfur compounds, but there is no evidence of active microbial activity, i.e., observations of significant fractionation in ^{34}S for sedimentary rocks, to trace bacterial cycling of sulfur in the Mesoarchean. Thus, further research is needed to gain clarity on this issue.

There is now a unique opportunity to identify different microbially driven processes and sulfur cycling on the early Earth due to multiple sulfur isotope (^{32}S, ^{33}S, ^{34}S, and ^{36}S) measurements and the existence of mass-independently fractionated sulfur isotope signatures (non-zero $\Delta^{33}S$ and $\Delta^{36}S$ values) in sediments older than 2.4 Ga [26,27]. The presence of non-zero values for $\Delta^{33}S$ and $\Delta^{36}S$ in ancient sedimentary rocks may reflect photochemical gas-phase reactions of volcanogenic sulfur dioxide (SO_2) in an anoxic atmosphere [28,29], which were responsible for the formation of a negative $\Delta^{33}S$-reservoir of sulfate and a positive $\Delta^{33}S$-reservoir of elemental sulfur [30]. The observations of negative and/or positive $\Delta^{33}S$ values in Archean sedimentary pyrite may be helpful for identifying different sources of sulfur that would have been involved in microbially driven processes. Revealing the correlation between $\Delta^{33}S$ and $\Delta^{36}S$ values may be especially helpful to make a differentiation between mass-dependent and mass-independent processes [31].

In this contribution, we present a study of sulfur isotope composition ($\delta^{34}S$, $\Delta^{33}S$ and $\Delta^{36}S$) of sulfides from the Mesoarchean volcanic-hosted massive sulfide occurrences in the southeastern part of the Karelian Craton by using laser-ablation sulfur isotope analyses. This study was performed in order to elucidate the sources of sulfur and the possible participation of bacteria in the transformation of sulfur to sulfides for occurrences of Mesoarchean age. Isotope data obtained in our work and their interpretation unequivocally indicate that microbially driven processes operated in Mesoarchean sedimentary environments, including two types of microbial sulfur metabolism–sulfate reduction and sulfur disproportionation.

2. Geological Setting

The Karelian Craton (Figure 1A) is the largest block of the Archean crust of the Fennoscandian (Baltic) Shield. It is formed by typical Archean granite–greenstone association and consist of granite–gneiss, greenstone, paragneiss and granulite complexes [32–36].

Three subprovinces are distinguished within the Craton: Vodlozero, Central Karelia and West Karelia, each possessing unique development characteristics during the Archean [35,37,38].

The Paleo- (3.3–3.1 Ga) and Meso-Archean tonalite-trondhjemite-granodiorite (TTG) gneisses and Mesoarchean (3.05–2.8 Ga) greenstone complex formed Vodlozero subprovince [34,42]. The Sumozero-Kenozero greenstone belt is located in the eastern part of it. It is one of the largest greenstone belts of the subprovince. It extends for ~400 km and is up to 50 km in width [34,39,41]. This greenstone belt is a system of the tectonic sheets and consists of slightly metamorphosed volcanic, volcanic-sedimentary, and intrusive rocks. Paleoproterozoic basaltic overlies the Archean sequence [35,41].

The Kamennoozero belt is one of the Sumozero-Kenozero greenstone belt fragments (Figure 1B). It includes two main units (tectonic sheets) with a total thickness of ~5 km [34,39]. The lower unit consists of pillow metabasalts and komatiite showing an affinity to oceanic plateau volcanism. The ages of this lower unit are 2892 ± 130 (by Pb-Pb) and 2916 ± 117 Ma (by Sm-Nd) [39]. The upper unit consists of volcanic basalt–andesite–dacite-rhyolite (BADR)-series rocks, bearing arc signatures, and adelite-series subvolcanic rhyolites. This volcanic

rock age is 2875 ± 2 Ma (by U-Pb zircon TIMS) [39]. The unique feature of the upper unit is the presence of sulfide ores [40,43,44], which served as the object of this study.

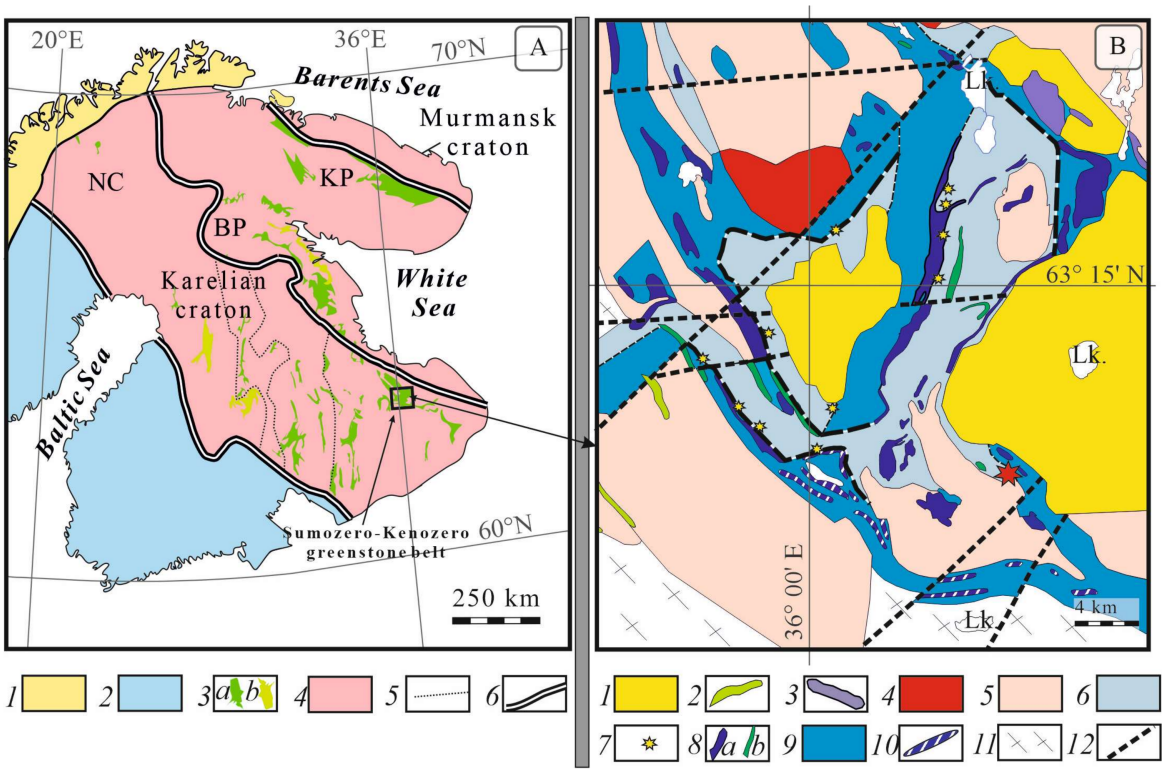

Figure 1. (**A**) Map showing the tectonic division of the Fennoscandian shield and the location of the Sumozero-Kenozero greenstone belt [35,36]. 1—Baikalids and Caledonides; 2—Paleoproterozoic juvenile crust; 3—Archean greenstone (**A**) and paragneiss (**B**) complexes; 4—Archean crust; 5—The Karelian Craton subprovince boundaries; 6—boundaries of Paleoproterozoic orogens. Letter abbreviation: KP—Kola Province, BP—Belomorian Province; NC—Norrbotten Craton. (**B**) Geological sketch map of the Kamennoozero greenstone belt and locations of ore deposits indicated by stars. Red star indicates the location of the studied Leksa deposit [34,39–41]. 1–3—Paleoproterozoic (Sumian): 1—basaltic andesite; 2—gabbro; 3—ultrabasite; 4–10—Archean: 4—Neoarchean granite; 5—Archean diorite, granodiorite, and tonalite; 6—Mesoarchean BARD- and Adakitic-series sedimentary-volcanic rocks interlaying with interbedded pyrite; 7—pyritic ore occurrences; 8—Mesoarchean (**A**) ultramafite and (**B**) gabbro; 9—Mesoarchean tholeiitic basalt; 10—Mesoarchean komatiite; 11—Paleo-Mesoarchean TTG-gneiss; 12—faults.

At the end of the last century, over 10 sulfide deposits were explored in the Kamennoozero belt by exploratory drilling (see Figure 1B). The volcano-sedimentary massive sulfide (VSMS) Leksa deposit studied here is located in the southeastern part of the Kamennoozero belt and occurs in strata of quartz–albite–sericite and shungite-bearing schists [40].

The carbon-bearing schists are made of thin veinlets and lenses of quartz and ferruginous chlorite in a fine-grained matrix built by a mixture of chlorite, quartz, muscovite, and shungite. Quartz–albite–sericite schists are metasomatic rocks, presumably former volcanogenic-sedimentary arc-type rocks [40]. Their mineral composition varies from carbonate–quartz–albite–sericite–chlorite to quartz–pyrite. Carbonate is found almost everywhere, which is characteristic of carbon-dioxide metasomatism.

Sulfide ores constitute several superimposed ore bodies (Figure 2) that formed two main sulfide-bearing sequences totally up to 40 m thick. Host rocks near the ore body underwent an intensive silicification. Sulfides are represented mainly as pyrite forming different morphological shapes (cubic crystals, framboids, rounded globules, and

layered concretions), rarer as pyrrhotite, chalcopyrite, sphalerite, and galena. Ores are impregnated, spotted, banded, massive, sometimes with veinlets, and of mainly pyritic composition 30%–50% of which are sulfides. The concentration of polymetals in ores is low (Zn 0.03%–0.24%; Au 0.003–0.06 ppm, Ag up to 0.02–4.00 ppm) [45]. The mineralization is characterized by being stratiform and associated with island-arc sedimentary-volcanogenic felsic rocks. Mafic lavas were not found by drilling, although field observations and the presence of fuchsite in metasomatites indicate their presence somewhere nearby.

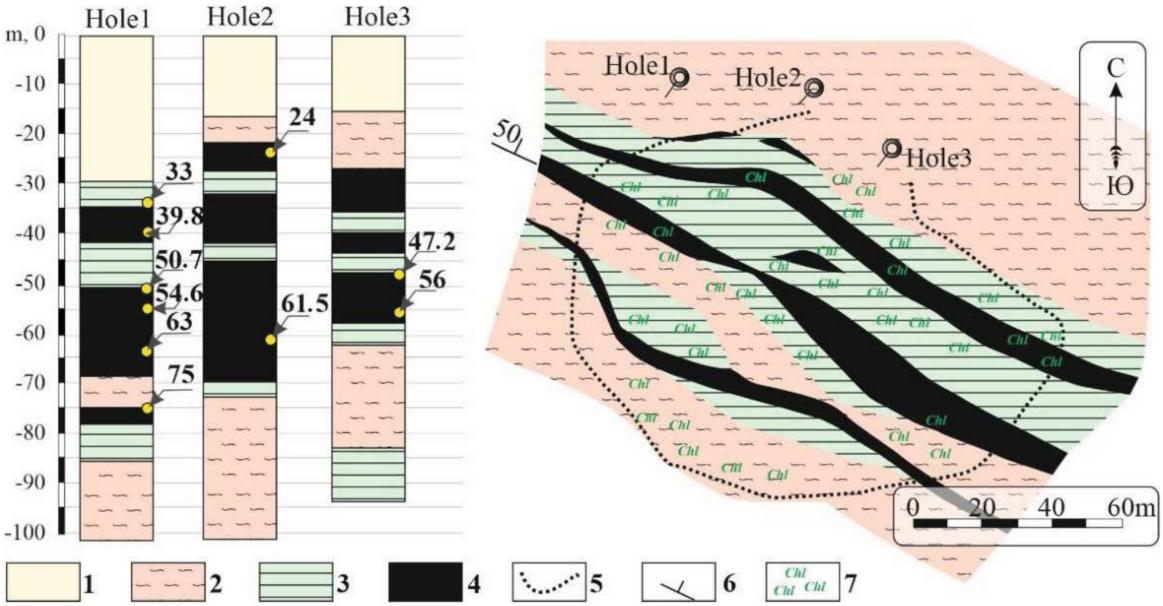

Figure 2. Geological sketch map of the Leksa deposit (compiled using the data of Kuleshevich (1992) and Kuleshevich et al. (2005) [40,41] with some modifications and additions). 1—Quaternary sediments, 2—quartz–carbonate–albite–sericite schists, 3—carbon-bearing schists, 4—sulfide ores, 5—silicification zone, with chloritoid blastesis (Chl), with fuchsite, 6—attitude, 7—metasomatic alteration zones (chloritization). Yellow dots on drillhole logs indicate sampling locations and depth below the surface.

Layered or banded, disseminated-banded and disseminated-streaky ore textures are usually typical for distal (distant from the hydrothermal discharge zone) facies of volcanogenic-sedimentary massive deposits [46]. Considering the established metal zonation at many VSMS deposits [47,48], the wells at the Leksa deposit possibly revealed rather low-temperature sulfide ore facies distant from the discharge hydrothermal zone. Based on the lithological classification of the host rock [49,50], we have classified this deposit as bimodal-mafic VSMS. Volcanic rocks of a VSMS deposit of this type are dominated by basalt, andesite, felsic lavas, and pyroclastic rocks. These deposits usually indicate hydrothermal fields related to island-arc volcanoes and backarc spreading centers [51].

3. Materials and Methods

Samples were collected from three drill cores: H1, H2, and H3. The cores intersect highly carbonaceous and carbonate–quartz–sericite shales. The choice of samples for the study was guided by the purpose of this research, which is to trace potential sulfur isotope signatures of Mesoarchean life. Therefore, sulfide samples were taken mostly from metasedimentary lenses in ore bodies of the Leksa deposit.

Two textural types of pre-metamorphic pyrite have been identified in these shales. Detailed sample descriptions are in Appendix, Figures A1–A5. One type is represented by aggregates of nano-micro crystals with different sizes, for which a generic term could be colloform-like pyrite. Colloform pyrite occurs as ellipsoidal aggregates composed of densely packed submicron-sized crystals and also as concentrically laminated grains. They are

common in both clay-carbonaceous and carbonate shales. An example of concentrically laminated grains presented in Figure 3A: pyrite layers alternate with layers of marcasite; interstitial spaces of the marcasite crystals are filled with chlorite (chamosite), sericite (muscovite), quartz crystals and graphite. Note that since our study does not address issues related to the conditions favorable for the formation of pyrite or marcasite, in further discussion of the results we use the term pyrite to refer both to pyrite and its polymorph, marcasite.

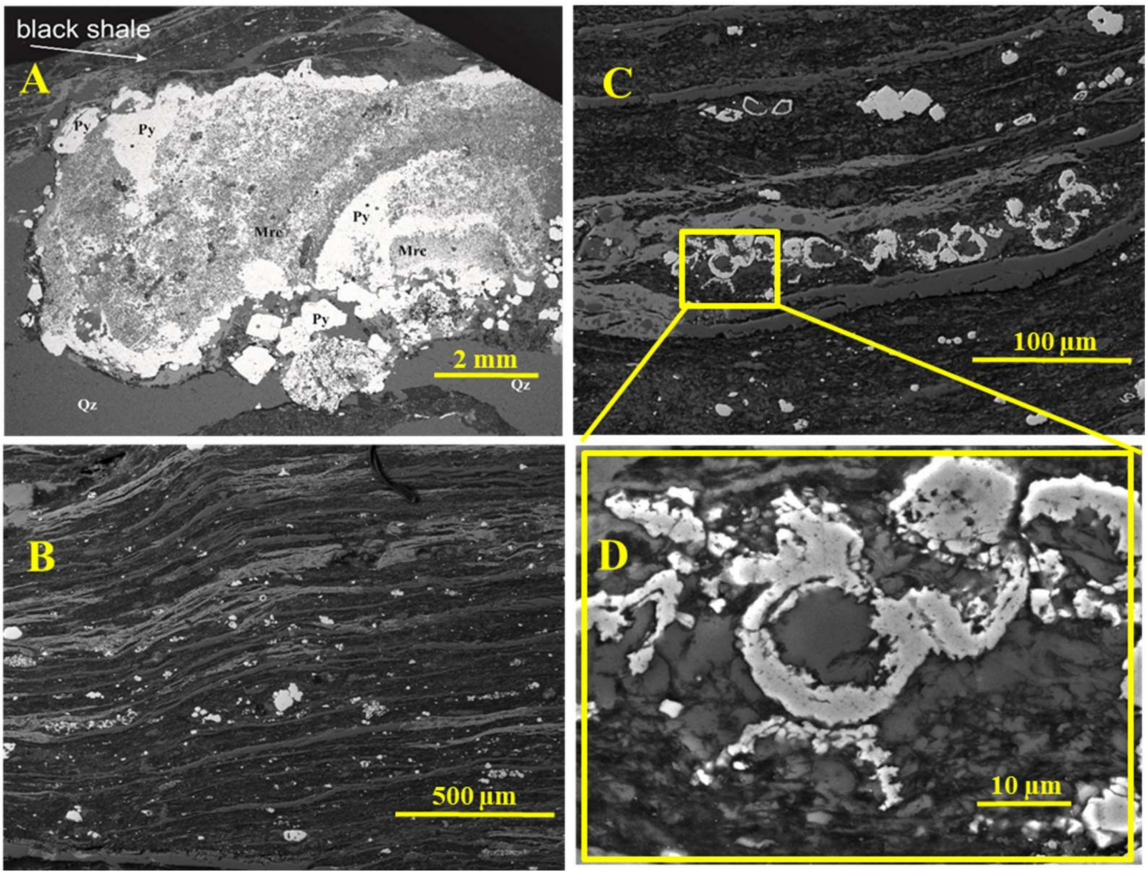

Figure 3. BSE images of pyrite grains from drill cores of the Leksa deposit: (**A**) concentrically laminated pyrite. Note that euhedral pyrite crystals (approximately 0.5 mm in diameter and less) occur around the laminated grain; (**B**) Disseminated euhedral pyrite crystals; (**C**) Micro-sized euhedral pyrite crystals observed as ring-shaped aggregates; Image (**D**) shows magnified view of marked area in (**C**).

Another type of pyrite (Figure 3B–D) studied here is represented by euhedral pyrite crystals. They commonly occur as individual microcrystals disseminated in the black carbonaceous shale (Figure 3B), or as thin layers composed of pyrite grains with a size of <100 µm. They also occur as aggregates of a few crystals with a size of ~0.5 mm that have overgrowth texture around concentrically laminated pyrite grains (Figure 3A). In some cases, pyrites were observed as ring-shaped and ball-shaped aggregates (typically less than 20 µm in diameter) of microcrystals, surrounding the inner core comprised of silicate minerals: quartz, chlorite, muscovite, or their mixture (Figure 3C,D).

From pyrite-bearing rock fragments of the drill-cores, polished chips (approximately 1–3 cm length/width and 0.5 cm deep) were prepared for both petrographic observation and isotope analyses. Samples used for isotope analysis were not subjected to additional processing, including etching in HNO_3. All analyses were performed at Far East Geological Institute FEB RAS in Russia. More details on sulfide petrography are provided in the Appendix A.

3.1. Sulfur Isotope Analysis

Femtosecond laser-ablation fluorination method described in detail in [52,53] was applied for in situ measurements of $\delta^{33}S$ and $\delta^{34}S$ values in sulfide minerals. Briefly, an ultraviolet femtosecond laser ablation system (NWR Femtosecond UC with laser Pharos 2mJ-200-PP and harmonics module HE-4Hi-A, supplied by Electro Scientific Industries New Wave Research Division, Portland, OR, USA) was used to produce a laser crater of approximately 80 µm diameter and 40 µm depth in pyrite. Laser-generated aerosol sulfide particles were converted to SF_6 (~12–13 nmol) via reaction with BrF_5 at 350 °C. The SF_6 was purified by means of a cryogenic trap system [53] and introduced into the ion source of a Thermo Scientific MAT 253 isotope ratio mass spectrometer using a gas injection interface developed and described in [52]. Sulfur isotope ratios were measured by monitoring the SF_5+ ion currents at mass to charge ratios of m/z 127 ($^{32}SF_5{}^+$), 128 ($^{33}SF_5{}^+$), 129 ($^{34}SF_5{}^+$), and 131($^{36}SF_5{}^+$).

It should be noted that it is not a problem if the size of the ablation pit is larger than the size of the analyzed sulfide grain because the presence of the matrix rock did not affect the accuracy and precision of analyses [53].

All sulfur isotope data are presented as conventional notation:

$$\delta = \frac{R_{sample}}{R_{standard}} - 1,$$

where R_{sample} and $R_{standard}$ are the $^{34}S/^{32}S$ or $^{33}S/^{32}S$ ratios for the sample and standard, respectively, and reported relative to Vienna Cañon Diablo Troilite (V-CDT). For describing sulfur isotope anomalies (mass-independent sulfur isotope fractionations), capital delta notation was used which is defined as follows [54]:

$$\Delta^{33}S = \delta^{33}S - \left[\left(\delta^{34} + 1\right)^{0.515} - 1\right]$$

$$\Delta^{36}S = \delta^{36}S - \left[\left(\delta^{34} + 1\right)^{1.90} - 1\right]$$

Three International Atomic Energy Agency standards (IAEA S1, S2, and S3) were used to calibrate the SF_6 reference gas and in-house standard. Analytical precision of ±0.2‰ (1σ) for $\delta^{34}S$ values, ±0.03‰ (1σ) for $\Delta^{33}S$ values, and ±0.27‰ (1σ) for $\Delta^{36}S$ values were estimated from the long-term (approximately 1-year-long period) reproducibility of in-house standard [53].

3.2. Scanning Electron Microscopy and Energy Dispersion X-ray Spectroscopy Analysis

- Scanning electron microscopy (SEM) was used to examine the detailed mineralogical and textural characteristics of sulfides on polished and some unpolished surface areas. Backscattered electron (BSE) and secondary electron (SE) imagery, as well as qualitative energy dispersive X-ray spectroscopy (EDS) analysis, was carried out on gold or carbon coated samples using a dual-beam TESCAN LYRA 3 XMH (Schottky cathode) Oxford AZtec Energy EDS system.
- Electron imagery was performed at variable acceleration voltage (20–30 kV) and beam current (9–14 nA). Up to 30 kV and 14 nA was used for EDS analysis to ensure sufficiently high peak count rates for accurate determination of characteristic element-specific X-ray emission lines.
- Quantitative X-ray spectroscopy spot analysis was performed using a JEOL JXA 8100 electron probe micro-analyser with three wave spectrometers and one energy dispersive spectrometers (Oxford Instruments Inca, Abingdon, UK), under a resolution of 137 eV MnKα, an accelerating voltage of 20 kV and a measure current of 1×10^{-8} A. Prior to analysis the samples were coated with a 20 nm carbon film. The beam was fully focused to give a spot size of about 1 µm with a measure current 1×10^{-8} A.

Pure metals, glasses, and minerals analyzed through other methods were used as standards along with Oxford Instruments standards. Total Fe is equivalent to Fe^{+2} in calculations.

- The qualitative phase analysis of sulfides was determined by X-ray diffraction in the powder by Rigaku MiniFlex II (Rigaku, Japan) (XRD) at the Laboratory of X-Ray Methods of the Analytical Center of the Far East Geological Institute, Far Eastern Branch of the Russian Academy of Sciences (FEGI FEB RAS) in Vladivostok.

4. Results

Sulfur isotope data are presented in Appendix A, Table A1 and displayed in Figure 4 as plots of $\delta^{34}S$ vs. $\Delta^{33}S$ values.

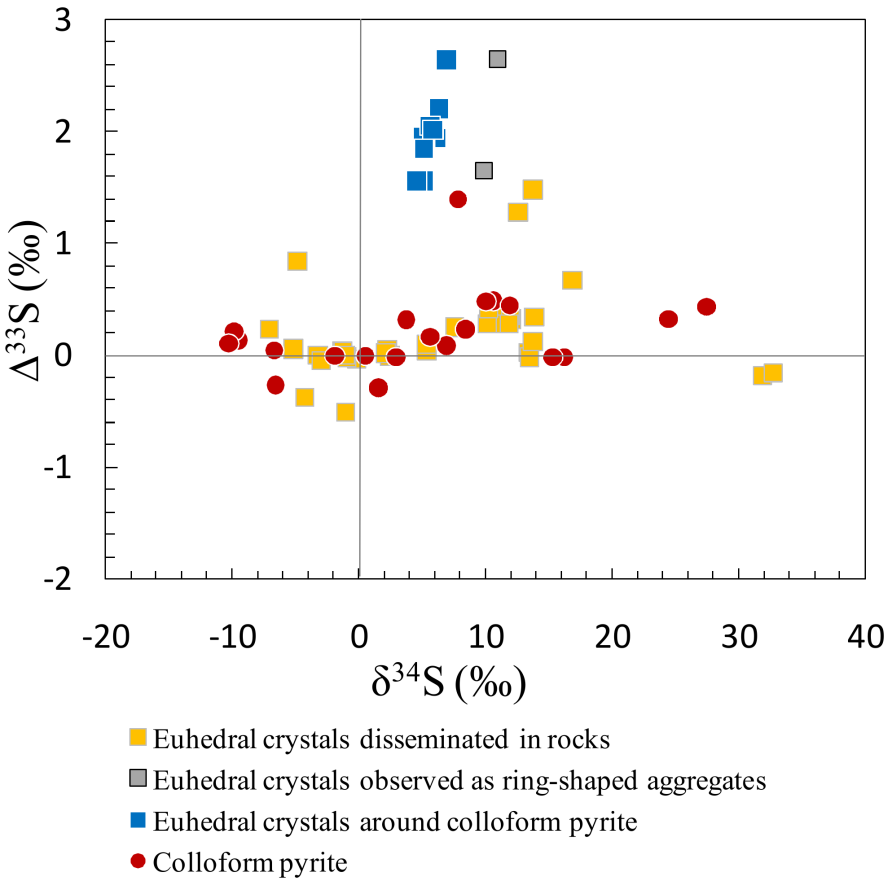

Figure 4. $\Delta^{33}S$ vs. $\delta^{34}S$ values for colloform and euhedral pyrite studied here. Data from Table A1 in Appendix A. Uncertainties for the data shown are smaller than the symbol sizes for $\delta^{34}S$ and $\Delta^{33}S$.

Colloform pyrite shows both negative and positive $\delta^{34}S$ values; a total $\delta^{34}S$ range is from −10.2‰ to +27.5‰ (Figure 4). In situ analyses revealed strongly heterogenous $\delta^{34}S$ values, ranging from −6.7‰ to +27.5‰ in concentrically laminated pyrite grains, and relatively homogenous $\delta^{34}S$ values that range from −10.2‰ to −9.5‰ and from −6.6‰ to +7.0‰ in non-laminated pyrite grains (Appendix A, Table A1). It is also evident that colloform pyrite studied here is mass-independently fractionated, with $\Delta^{33}S$ values that mainly vary between −0.3‰ and +0.5‰. The exception is relatively large positive $\Delta^{33}S$ = +1.4‰ measured in the core of the concentrically laminated pyrite (see Appendix A, Figures A4 and A5).

The euhedral pyrite crystals have showed a wide spread of $\delta^{34}S$ values and also revealed the presence of mass-independently fractionated sulfur. More specifically, disseminated pyrite exhibited intergranular heterogeneity for $\delta^{34}S$ and $\Delta^{33}S$ values that vary

between −7.0‰ and +32.7‰ and between −0.5‰ and +1.5‰, respectively (Figure 4). These data are similar to those obtained for concentrically laminated pyrite grains. In contrast, euhedral pyrite overgrowths observed around colloform pyrite are relatively homogeneous in $\delta^{34}S$ and $\Delta^{33}S$ values that vary between +4.6‰ and +7.0‰ and between +1.5‰ and +2.7‰, respectively (Figure 4). Two analysis of euhedral pyrite observed as ring-shaped and ball-shaped aggregates of microcrystals have showed $\delta^{34}S$ = +11.0‰ and +9.9‰, $\Delta^{33}S$ = +2.7‰ and +1.7‰ (Table A1, Figure 4).

A subset of the euhedral pyrite samples was measured for $^{36}S/^{32}S$ isotope ratios to understand the relationship between $\Delta^{33}S$ and $\Delta^{36}S$ values. These pyrite grains have negative $\Delta^{36}S$ values which range from −1.3 to −2.5‰ (Table A1), and also show a negative correlation between $\Delta^{33}S$ and $\Delta^{36}S$ with a slope of ≈−1.15 (Figure 5).

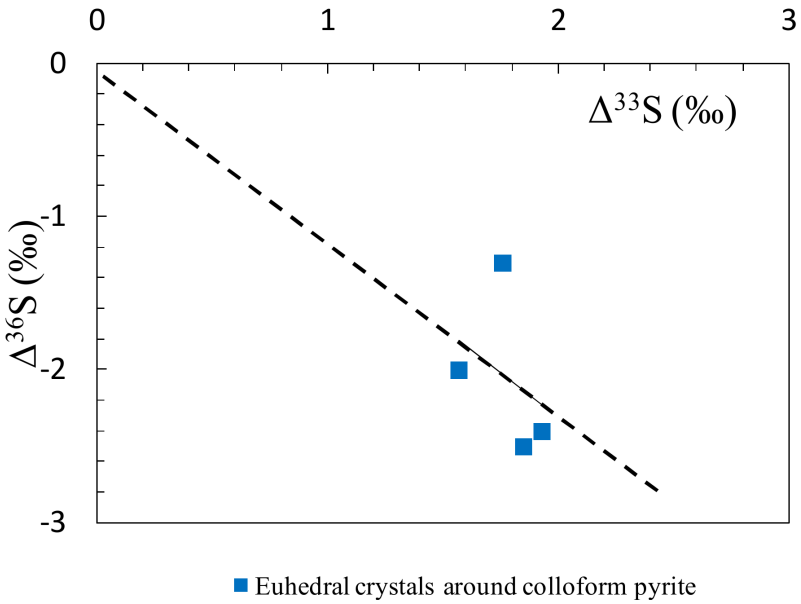

Figure 5. $\Delta^{36}S$ vs. $\Delta^{33}S$ values for a subset of the euhedral pyrite samples. Data from Table A1 in Appendix A. The dashed line is linear fit to data with a slope of −1.15.

5. Discussion

As pointed out earlier in the introduction, the range of variability for $\delta^{34}S$ values of sulfides from the Mesoarchean rocks represented by sedimentary units in southern Africa [22–24] and Western Australia [22] is significantly smaller compared to other Archaean intervals. Sulfur isotope data reported in this study, however, reveal a much wider range of $\delta^{34}S$ values (−10.2‰ to +32.7‰) in the 2.8 Ga old rocks of the Karelian Craton (Figure 6). Figure 4 also illustrates one feature of the sulfur isotope record identified in our study, which is the presence of relatively high $\Delta^{33}S$ values between +1.5‰ and +2.7‰ in the euhedral pyrite grains and the relatively low $\Delta^{33}S$ values mostly between −0.30‰ and +0.44‰ for the colloform pyrite.

These observations aroused an obvious research interest regarding the possible pathways to differentiate the sulfur isotope ratios between these texturally distinct types of pyrite. Moreover, can the sulfur isotope data be explained in terms of known microbial processes and what these data tell us about the Mesoarchean microbial life? We suggest that considering what we know today about pyrite formation in modern sedimentary environments and sulfur isotope fractionation associated with microbial processes may help in answering these questions.

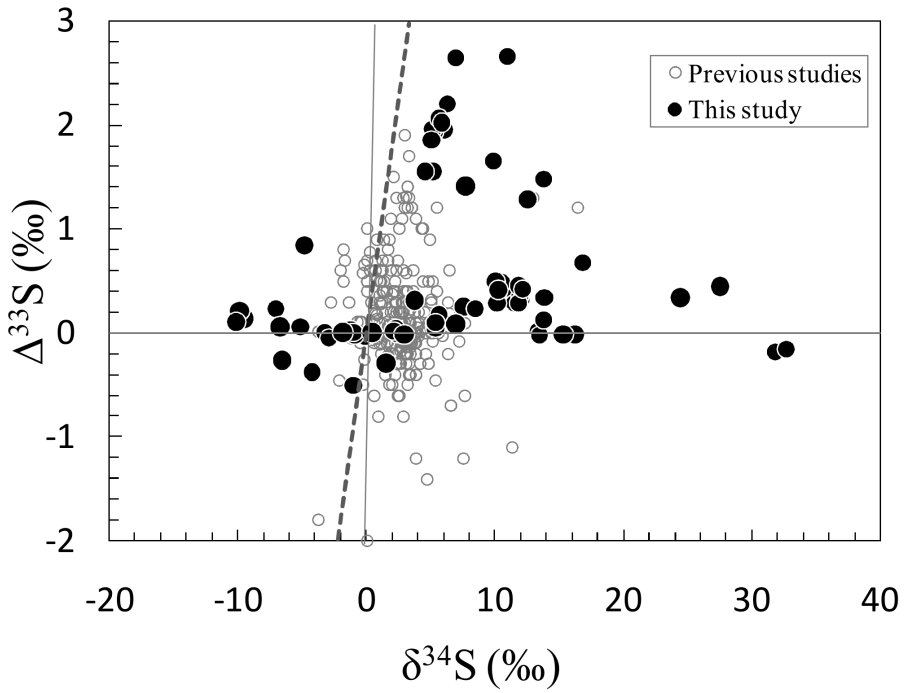

Figure 6. The Mesoarchean sedimentary sulfide $\delta^{34}S$ and $\Delta^{33}S$ data. Grey unfilled circles are literature data for Mesoarchean samples from Southern Africa and Western Australia [23,26,31]. Filled black circles are data representing in this study in Table A1. Also shown is the dashed line represented the Archean reference array ($\Delta^{33}S = 0.9\ \delta^{34}S$).

A possible mechanism of pyrite formation has been studied in several experimental works [55–57]. The formation of low-temperature sedimentary pyrite can occur in an anoxic environment and is mainly initiated by the reaction of dissolved H_2S with reactive iron to yield non-crystalline monosulfide:

$$Fe^{2+} + H_2S \rightarrow FeS + 2H^+ \quad (1)$$

The produced FeS is a transit product in the process of pyrite formation. There are two ways to transform FeS to pyrite: by the reaction of FeS with elemental sulfur

$$FeS + S^0 \rightarrow FeS_2, \quad (2)$$

or by the reaction of FeS with H_2S

$$FeS + H_2S \rightarrow FeS_2 + H_2. \quad (3)$$

5.1. Sulfur Pathways Recorded by the Studied Colloform Pyrite

In our work it can be expected, as a first approximation, that dissolved H_2S which is needed for pyrite formation in marine sediments could be produced primarily from sulfate dissolved in sea water by microbial metabolism that operated at the time of pyrite deposition. This is because the wide range from −6.7‰ to +27.5‰ and strong isotopic heterogeneity in $\delta^{34}S$ values observed at micrometer scale in our sample of concentrically laminated pyrite grains (Figure A4, Appendix A) could be attributed to biological sulfate reduction, as the most likely mechanism to produce very large fractionation of sulfur isotopes [13].

We note that colloform pyrite studied here by in situ isotope analysis displays both positive (up ~1.4‰) and negative (−0.30‰) $\Delta^{33}S$ values (see Figure 4). Distinct mass-independent sulfur isotope signals may indicate the transformations of sulfur species in

the oxygen-poor atmosphere via photochemical reactions of volcanogenic SO_2 [26]. These ultraviolet-driven reactions should, according to photochemical experiments [58–65], produce sulfate aerosols with a negative $\Delta^{33}S$ signature and elemental sulfur aerosols with a positive $\Delta^{33}S$ signature. As a result of SO_2 atmospheric photochemistry, two compositionally and isotopically distinguished photolytic sulfur pools can be generated and maintained in an anoxic atmosphere. The absence of free molecular oxygen in the atmosphere prevents the oxidation of elemental sulfur to sulfate, and hence the homogenization of the mixing of different pools. An anoxic atmosphere favors the coexistence of various photolytic sulfur reservoirs and transfers the photolytic components out of the atmosphere to Earth's surface. Once atmospherically derived elemental sulfur and sulfate rained out into aquatic environments, they can then be transformed into pyrite which inherits the isotope anomaly. Since the samples of colloform pyrite studied here archived opposite signs of the sulfur isotope anomaly, we can suggest photolytic seawater sulfate and photolytic elemental sulfur to be the principal sulfur source during precipitation of the pyrite grains with colloform texture.

According to the above consideration, isotope characteristics of colloform pyrite samples (i.e., non-zero $\Delta^{33}S$ values, the broad range and also strong isotopic heterogeneity in $\delta^{34}S$ values) may be associated with photolytic origin of its sulfur and would be consistent with forming pyrite via microbially mediated pathways, namely photolytic sulfate converted to H_2S through microbial sulfate reduction. However, it needs to be ascertained if unusually high $\delta^{34}S$ values of the studied pyrite can be associated solely with microbial sulfate reduction.

5.2. Colloform Pyrite—A Result of Microbial Sulfate Reduction Alone?

Based on current knowledge of sulfur isotope fractionations between sulfate and sulfide by bacterial sulfate reduction, the produced H_2S is ^{32}S-enriched vs. parent sulfate (i.e., $\delta^{34}S_{sulfide} < \delta^{34}S_{sulfate}$) [13,66–70]. If continued sulfate reduction takes place within a restricted system (in sediment pore waters), the concentration of sulfate in the system falls and Rayleigh fractionation occurs. As a result, the common sulfur isotopic trend observed for both remaining sulfate and pyrite formed is that $\delta^{34}S$ values progressively increase as sulfate is consumed by sulfate-reducing microorganisms [71,72]. Therefore, the simplest explanation for the high-$\delta^{34}S$ values (up to +27.5‰) observed in the concentrically laminated pyrite grains would be restricted-reservoir effects. In this situation, formation of these grains may take place along or below the sediment-water interface, not within the marine water column with a relatively large pool of available sulfate in comparison to sediment pore water, and thus Rayleigh fractionation is unlikely to occur. A sedimentary origin for the pyrite grains is also supported by preservation of their textural characteristics. Pyrite grains with concentric texture have been reported for Precambrian sedimentary successions and extensively reviewed [73]. This type of pyrite is interpreted to have formed in shallow-marine environments through accretion of pyrite mud [74,75], so the growing and aggregation of microcrystals from the inner core to the outer concentric layers can be explained by geometrical selection [76].

Concentrically laminated pyrite grains from sedimentary rocks of the Witwatersrand Basin in the central Kaapvaal Craton (South Africa) have been interpreted by Agangi and coauthors [77] to have formed at the water–sediment interface and their $\delta^{34}S$ values that range from −12.2‰ to +12.6‰ have been considered as a result of sulfur isotope fractionation during sulfate reduction accompanied by Rayleigh fractionation in a closed system (at constant sulfate−sulfide fractionation). According to these authors, more than 80% of available sulfate must be consumed by sulfate reducers, which may lead to formation of pyrite with the highest (+12.6‰) $\delta^{34}S$ values (under the assumption that an initial $\delta^{34}S$ of the fluid ~−1‰). In our work, concentrically laminated pyrite grains from the Leksa deposit in the eastern part of Karelian Craton have been observed to have the $\delta^{34}S$ values as high as +27.5‰, that is ~15‰ higher in comparison to Witwatersrand concentric pyrite [77]. Although one feasible explanation we propose for the strongly ^{34}S-enriched sulfides is

microbial processes, it remains unclear whether such isotopic enrichments can be achieved only through microbial sulfate reduction, even in restricted pore waters.

To calculate the magnitude of the ^{34}S isotopic enrichment in sulfide during bacterial sulfate reduction undergoing Rayleigh-type distillation in a closed system, the equation from [78] was used. We made some assumptions regarding the initial conditions in our calculations. They are: (1) starting concentration of marine sulfate was taken as 200 μM, following the conclusions of [79] that "oceanic Archean sulfate concentrations were <200 μM", although much lower sulfate levels ≈80 μM [80] and even <10 μM are also possible [21,81]; (2) the initial marine water sulfate had a $\delta^{34}S$ value of ~0‰ [82]; (3) the fractionation associated with sulfate reduction was taken as 10‰ (i.e., $\delta^{34}S_{sulfate} - \delta^{34}S_{sulfide} \approx 10‰$), since the maximum depletion of ^{34}S into pyrite observed in our study is ~−10‰. If other mechanisms did not operate, the calculations show that more than 98% of the total sulfate in the system should be consumed by bacteria to explain pyrite highly enriched in ^{34}S up to ~ +27‰. In this case the residual sulfate concentration may expect to be <4 μM, which is too low to enable bacterial sulfate reduction because threshold concentrations for sulfate uptake have been detected at ~5 to 20 μM sulfate [83]. Thus, the current model does not provide an explanation for the high $\delta^{34}S$ values measured in concentrically laminated pyrite grains.

To elucidate the possible reasons for the formation of highly ^{34}S-enriched pyrite, other cases can be considered. It is possible that the sulfur isotopic composition of Archean seawater sulfate could be higher than 0‰. Then a Rayleigh distillation model will require the $\delta^{34}S$ value of seawater sulfate to be not less than ~+10‰ to generate pyrite with $\delta^{34}S \approx +27‰$ upon removal of 85% of sulfate by sulfate-reducing microorganisms in the hypothetically closed system. These considerations are in line with [84] that the $\delta^{34}S$ of Archean seawater sulfate may be in the range of +6‰ to +16‰. However, this is not the case for our samples since our model calculations with large sulfur isotope fractionations between hydrogen sulfide and sulfate of more than 25% should imply high sulfate concentrations of the Mesorchean ocean, but there exists no evidence to support this resulting deduction.

5.3. Colloform Pyrite: Evidence of Sulfur Disproportionation Accompanying Sulfate Reduction

Here we demonstrate that observed high $\delta^{34}S$ values in colloform pyrite can be explained by mixing two different pools of sulfate available simultaneously for sulfate-reducing bacteria at the site of pyrite formation. One of these pools was dissolved atmospherically derived photolytic sulfate, and the other pool was biologically produced sulfate, namely as a result of microbial disproportionation of atmospherically derived insoluble elemental sulfur. Microbial elemental sulfur disproportionation in marine sediments served as the source of sulfate and hydrogen sulfide in the pore water [85,86]:

$$4S^0 + 4H_2O \rightarrow 3H_2S + SO_4^{2-} + 2H^+ \quad (4)$$

It was shown that bacterial sulfur disproportionation results in generating sulfide that is depleted in ^{34}S only up to 7‰ while sulfate is enriched in ^{34}S up to 30‰ relative to starting sulfur [86–92]. Then, the combination of microbial sulfur disproportionation and microbial sulfate reduction can be proposed to explain highly positive $\delta^{34}S$ values of pyrite studied here. If sulfate reduction takes place and sulfate derived from elemental sulfur is continuously added to the reservoir, pyrite produced from the sulfate mixture can reach a high positive $\delta^{34}S$ value even before the concentration of available sulfate in the pore water drops to a threshold of ~5 to 20 μM [83] and pyrite formation ceases. This interpretation suggests that pyrite was formed in sediments high in available elemental sulfur for microbial processes where elemental sulfur delivered from the atmosphere consistently fell to the bottom and accumulated in sediments, forming the elemental sulfur pool. Metabolism of elemental sulfur by bacteria resulted in the formation and maintenance of a biologically derived sulfate pool, which mixed with the atmospherically derived sulfate pool that contained within pore waters of the sediment. This process was

accompanied by the metabolism of sulfate sulfur through sulfate-reducing bacteria to form pyrite. If so, disproportionation of atmospherically derived elemental sulfur in the sediment would act as a source of additional sulfate in the processes of continuous loss of atmospherically derived sulfate by bacteria out of the pore waters in the closed system. This would be running into the changes in $\delta^{34}S$ values that can be observed in different pyrite grains because their $\delta^{34}S$ values should be related directly to the concentration of available biologically and atmospherically derived sulfate in pore water. Pyrite exhibiting negative $\delta^{34}S$ values would be expected if a greater proportion of total sulfate reservoir would be atmospherically derived sulfate with $\delta^{34}S$ values of ~0‰. Pyrite exhibiting relatively high $\delta^{34}S$ values would be apparent if the $\delta^{34}S$ values of sulfate reservoir would have been locally increased due to metabolism by sulfate-reducing bacteria, where the loss of the sulfate in a closed system would be replenished from a pool of atmospherically derived elemental sulfur through bacterial metabolism of elemental sulfur.

It should be noted that a combination of sulfate reduction and sulfur disproportionation has been proposed to explain strong ^{34}S depletions in sedimentary sulfides [86,93]. Indeed, these processes may be responsible for formation of depleted rather than enriched ^{34}S sulfides, but only if the mechanism of sulfide oxidation into elemental sulfur is involved [86,93], implying the presence of an oxidizing environment. We consider such an environment unlikely to exist at the time of deposition of pyrite studied here, because it is inconsistent with the observed significant mass-independent isotopic signals in pyrite, generation and preservation of which requires an anoxic depositional environment [84].

If our assumption linking formation of colloform pyrite and two different metabolic pathways of sulfur is true, colloform pyrite should also be highly inhomogeneous at micrometer scale in the $\delta^{34}S$ values. This is because the magnitude sulfur isotope fractionation induced by bacteria, and hence pyrite $\delta^{34}S$ value, depends on microbial sulfate reduction rates, which in turn can be related directly to the concentration of available dissolved sulfate as well as organic matter. Therefore, in microenvironments where several biologically mediated mechanisms operate simultaneously, produced pyrite can be remarkably heterogeneous in $\delta^{34}S$, which was observed for concentrically laminated pyrite grains studied here.

Proceeding from our assumption of a biogenic origin for pyrite genesis, the presence of two different metabolic pathways should be responsible not only for the local variations in $\delta^{34}S$ values, but also for $\Delta^{33}S$ values, which is the case for the samples of colloform pyrite. Concentrically laminated pyrite grains are characterized by a heterogeneous distribution of nonzero $\Delta^{33}S$ values as well as the presence of zero $\Delta^{33}S$ values.

The observed at micrometer scale changes in $\Delta^{33}S$ values of pyrite grains cannot be explained by microbial activity and associated Rayleigh fractionation of sulfur isotopes in restricted pore waters. It is because bacterial sulfate reduction and sulfur disproportionation cannot induce sulfur isotope mass-independent fractionation; the transformation of sulfur by these processes cannot significantly change $\Delta^{33}S$ of sulfur reservoirs. In other words, as bacterial sulfate reduction with Rayleigh distillation progressively occurs within a $\Delta^{33}S$-bearing reservoir, the $\Delta^{33}S$ magnitude of the remaining sulfate reservoir remains unchanged and, thus, pyrite formed should be homogeneous in $\Delta^{33}S$ values and identical to the $\Delta^{33}S$ reservoir.

Strong heterogeneity in $\Delta^{33}S$ at the micrometer scale that we observe for colloform pyrite can be explained by relatively rapid alteration of $\Delta^{33}S$ for sulfur reservoir due to mixing in pore waters at least two sulfate reservoirs that should carry isotopic distinguishing $\Delta^{33}S$ signatures. In the present study it is suggested that the negative $\Delta^{33}S$ reservoir of sulfate available for use by sulfate-reducing microorganisms in pore water could have been diluted by positive $\Delta^{33}S$ sulfate, which was produced through bacterial sulfur disproportionation of atmospherically derived elemental sulfur accumulated in sediments. In this case, the relative bacterial sulfur disproportionation rates would locally influence and alter the integrated $\Delta^{33}S$ signature of dissolved sulfate in pore waters. Thereby a change in the $\Delta^{33}S$ value of local sulfate reservoir gives rise to a change in the pyrite from negative

to positive $\Delta^{33}S$ values, including zero $\Delta^{33}S$ values. Microbial activity can be seen as a mixer if the amount of elemental sulfur was not a limiting factor for pyrite formation. This means that the presence of $\Delta^{33}S$ values close to zero within concentrically laminated pyrite grains studied here does not necessitate an origin of sulfur from magmatic inputs but may result from mixing of two $\Delta^{33}S$-distinct sulfate reservoirs. It is conceivable that the simultaneous operation of two different metabolic pathways led to the erasing of the atmospheric signature in the pyrite studied here.

An additional issue with the existence of mass-independent isotopic signals in our samples arises: whether the observed $\Delta^{33}S$ values in the sample of colloform pyrite are attributable to the photolytic origin or it may be due to kinetic sulfur isotope fractionation associated with metabolic pathways.

According to experimental and modeling studies, the positive difference between $\Delta^{33}S$ values of sulfide and sulfate up to 0.2‰ are produced by microbial sulfate reduction (if only large isotope fractionations in $\delta^{34}S$ of >30‰) and slightly negative or positive shifts in $\Delta^{33}S$ values are associated with microbial sulfur disproportionation [31,92,94–96]. In our work isotopic data obtained for the grains with concentric texture are very difficult to associate with a purely kinetic sulfur isotope fractionation, since the magnitude detected for $\Delta^{33}S$ values is too large (>0.3‰) to account for the shift in $\Delta^{33}S$ due to microbial sulfate reduction. According to the above discussion, microbial sulfate reduction in combination with microbial sulfur disproportionation can explain both the highest $\delta^{34}S$ values (+27‰) and strong variability of the $\delta^{34}S$ and $\Delta^{33}S$ values measured in concentrically laminated pyrite grains at the micrometer scale.

5.4. Euhedral Pyrite: Evidence of Sulfur Disproportionation Accompanying Sulfate Reduction

The hypotheses presented here make it possible to understand what the reason is for a drastic increase in the $\Delta^{33}S$ values of up to +2.7‰ in euhedral pyrite grains developed around the colloform pyrite (see Figure 4) and why these euhedral grains are so homogeneous in both $\delta^{34}S$ and $\Delta^{33}S$ values. These questions deserve special consideration because euhedral pyrites were formed later than the colloform pyrite but yield higher $\Delta^{33}S$ values compared to colloform pyrite formed at an early stage of diagenesis. It would seem that an additional source of sulfur carrying a positive signal appeared in the system, for example, due to the opening of the system during late diagenesis. This scenario assumes infiltration of atmospherically derived sulfur carrying $\Delta^{33}S > 0$‰ towards the site of pyrite formation, which is unlikely because elemental sulfur is an insoluble component of sediments. Instead of this we consider a closed system where the amount of atmospherically derived elemental sulfur being accumulated in the sediment was sufficient to form pyrite. Very distinct multiple sulfur isotopic signals of euhedral and colloform pyrite would simply be the result of the exhaustion of atmospherically derived sulfate within pore waters at the time when formation of euhedral pyrite occurred within sediments.

Based on the formation mechanism of early and late diagenetic pyrites, the sequence of processes that may be responsible for the isotopic features observed in different pyrite generations is proposed as follows:

(1) During early diagenesis, the main mechanism of pyrite formation with concentric texture could, as considered above, be closely related to the transformation of photolytic sulfates and elemental sulfur to pyritic sulfur by microbial processes, and therefore these pyrite grains showed the large range of variability for both $\delta^{34}S$ and $\Delta^{33}S$ values;

(2) As diagenesis continues during burial, diffusion of dissolved sulfate into marine sediments from overlying water decreases thereby limiting sulfate reducers activity. In this situation, the residual photolytic elemental sulfur could be a dominant source for the formation of pyrite via reactions (R1−R3). Pyrite crystallization by this mechanism occurs only as aggregates of microcrystals ~1 μm in diameter [55];

(3) With the burial of sediment, the processes of recrystallization and overgrowth of the microcrystals can result in the formation of large euhedral pyrites [97–99]. Accordingly, the euhedral pyrites issued by these processes were observed around the concentrically

laminated pyrite grains. The remarkable intergranular and intragranular homogeneity in both $\delta^{34}S$ and $\Delta^{33}S$ values as well as large positive magnitude of $\Delta^{33}S$ values inherited from photolytic elemental sulfur are reasonably expected in these pyrites.

It is worthwhile saying that the strongly positive $\Delta^{33}S$ observed here for euhedral pyrite grains undoubtedly reflects the presence of mass-independently fractionated sulfur. Atmospheric origin of this sulfur was proven by including $\Delta^{36}S$ in the analysis. It was revealed that the values of $\Delta^{33}S$ linearly correlate with $\Delta^{36}S$ with a slope of ca. −1.15 (Figure 5), indicating an atmospheric source because the obtained slope differs from a slope of −6.85 (Figure A6), produced by mass-dependent microbially mediated processes [31], but is in good agreement with the Archean trend with a slope of −0.9 produced by mass-independently fractionated sulfur isotopes in Archean rocks.

Besides the concentrically laminated pyrite studied here, the single euhedral crystals or aggregates of a few crystals developed in fine-grained sedimentary rocks can also clearly indicate that sulfate-reducing and sulfur-disproportionating bacteria could have played an essential role at the time of deposition of these grains. This is because the large range of $\delta^{34}S$ values (−7.0‰ to +32.7‰) observed for the disseminated pyrite grains (see Figure 4) is consistent with the range in $\delta^{34}S$ variability from concentrically laminated pyrite (−6.7‰ to +24.5‰), and therefore could be explained by similar arguments that the formation of pyrite sulfur was closely related to the microbial processes of sulfate reduction, sulfur disproportionation, or a combination of both. The preservation of both positive and negative $\Delta^{33}S$ values in the euhedral pyrite crystals also implies the presence of at least two sources of sulfur for the formation of pyrite, that is, atmospherically derived sulfate carrying $\Delta^{33}S < 0$‰ and elemental sulfur carrying $\Delta^{33}S > 0$‰. An additional point to emphasize is that most of the disseminated pyrite grains analyzed in this work have moderate $\Delta^{33}S$ values ranging roughly between −0.3‰ and 0.5‰ (Figure 4). The exception is the cluster of crystals that form the ring-shaped or tubular structures (see Figure 3); they showed distinctively higher $\Delta^{33}S$ values of 1.65‰ and 2.65‰ (Figure 4). We associate these structures with the fossilization of microorganisms. Similar structures considered as evidence of microfossils have been described in Paleorchaean rocks of Western Australia [100], in Mesorchaean VSMS deposit in the Pilbara of Western Australia [101], in the Witwatersrand System of South Africa [102] and in Phanerozoic sediments [103]. An exhaustive review of microstructures that have been considered as Archean microfossilsis has recently been published by [104]. Experimental studies have shown that macroscopic structures of bacteria may be preserved by pyritization. This is shown by the presence of amorphous FeS on both the inner and outer surfaces of sulfate-reducing bacteria and by the immobilization of FeS around the bacterial microcolony [105]. Once FeS is formed it can transform into pyrite by the reaction of FeS with H_2S or S^0 (reactions R2-R3).

Based on the fact that $\Delta^{33}S$ values measured for pyritized fossils in this study were as high as +2.65‰, we are certain that elemental sulfur was the dominant source for the processes that are responsible for the pyritization of microorganisms. This, of course, does not mean that pyritized fossils were necessarily disproportionating microorganisms, but may be considered in favor of the latter.

5.5. General Insights

In summary, the mutually complementary facts considered in this study as evidence of the integrated activity of sulfate-reducing and sulfur-disproportionating bacteria rather than sulfate reducers alone at the time of pyrite formation are the following:

(1) The similarity of the isotopic composition of microfossils (average $\delta^{34}S \approx +10$‰ and $\Delta^{33}S \approx +2$‰) to that measured both in the core of concentrically laminated pyrite ($\delta^{34}S \approx +7.8$‰ and $\Delta^{33}S \approx +1.4$‰) and in the euhedral pyrite surrounding it (average $\delta^{34}S \approx +5$‰ and $\Delta^{33}S \approx +1.8$‰);

(2) The similar range of $\delta^{34}S$ variations, spanning between −7.0‰ and +32.7‰, for both dispersed and concentrically laminated pyrite that is too large to be interpreted as microbial sulfate reduction.

The importance of microbial sulfur disproportionation for early Archean pyrite formation is also evidenced by the multiple sulfur isotope data of Philippot and coauthors [4]. They suggested that the microscopic sulfides with negative $\delta^{34}S$ and positive $\Delta^{33}S$ values in barite deposit (Dresser Formation, Western Australia) are likely due to the activity at this time of the coexisting sulfur-disproportionating, sulfur-reducing and sulfate-reducing microorganisms. However, an alternative origin for this negative relationship between $\Delta^{33}S$ and $\delta^{34}S$ in microscopic pyrite has been proposed by Bao and his team [106]; that is, the mixing scenario where sulfides derived from S^0 (produced by the 193 nm SO_2 photolysis) and sulfides derived from seawater sulfate could be mixed in different proportions. Moreover, it is still possible that that the puzzle of isotopic effects will fit if sulfur-disproportionating bacteria that can also reduce sulfate were involved in the generation of the micropyrites [107].

Although the fact of the existence of microorganisms in the Archaean is well established today, less is known about the communities of bacteria which can utilize sulfur species for their metabolism in an Archaean environment. If the isotope data for sedimentary pyrite studied here indicate the coexistence of sulfur-disproportionating and sulfate-reducing microorganisms in the Mesoarchean, the sedimentary circumstances should be expected to favor the growth of both groups of these organisms. It is important that bacterial sulfur disproportionation is more sensitive to the hydrogen sulfide concentrations than bacterial sulfate reduction. In experimental studies [87,108] it was evidenced that utilization of elemental sulfur by disproportionating bacteria occurs only in the presence of a hydrogen sulfide scavenger because disproportionation of elemental sulfur is inhibited as the hydrogen sulfide concentrations raised >1 mM. In early anoxic oceanic environments with abundant Fe^{2+} in the Archean oceans [109], the presence of Fe^{2+} in pore water could act as a scavenger, buffering the hydrogen sulfide concentrations in pore water to low levels, even with rapid rates of bacterial sulfate reduction. Shallow lagoons could, according to [106], be favorable habitats for sulfur disporportionating bacteria before the rise of atmospheric oxygen. In addition, the mineral textures of pyrites studied here supports the assumption that the pyrite grains would have been formed in shallow water conditions in a zone away from the area where hydrothermal fluids vented onto the sea floor and where temperatures would have been low enough for the development of microbial activity.

6. Conclusions

A sulfur isotope study of sedimentary pyrite from Mesoarchean rocks of the Karelian Craton revealed signatures of mass-independent isotope fractionation and wide $\delta^{34}S$ variations in pyrite grains. Variations in the magnitude of $\Delta^{33}S$ values, in the range of −0.3‰ to +2.7‰, were close to those recorded in the rocks of similar ages in Southern Africa and Western Australia [22–24]. The negative and positive $\Delta^{33}S$ values observed in the present study were interpreted as a result of transferring photolytic sulfate and elemental sulfur to the sulfide sulfur in these samples; preservation of mass-independent signals in sedimentary rocks from the Karelian Craton supports the influence of atmospheric photochemistry on the sulfur cycling in the Mesoarchean [22].

The most striking features of the isotope data reported here are the remarkably large mass-dependent sulfur isotope fractionations where the $\delta^{34}S$ values extend from −10‰ to +32‰ and exceed previously reported $\delta^{34}S$ variations in Mesoarchean samples. In situ measurements of sulfide grains also reveal strong heterogeneity for both $\delta^{34}S$ and $\Delta^{33}S$ values. We argue that the source of these isotope effects was microbial processes, namely bacterial sulfur reduction in combination with microbial sulfur disproportionation. The present results can enhance understanding of sulfur cycling and microbial life in the Mesoarchean.

Author Contributions: Conceptualization, T.A.V. and S.V.V.; methodology, T.A.V. and A.V.I.; investigation, A.V.I. and A.V.A.; writing—original draft preparation, T.A.V., S.V.V. and A.V.A.; writing—review and editing, S.V.V. and A.I.S.; supervision, S.V.V.; project administration, S.V.V.; funding acquisition, S.V.V. All authors have read and agreed to the published version of the manuscript.

Funding: This work was supported by the Russian Science Foundation [grant number 21-17-00076, https://rscf.ru/project/21-17-00076/] (accessed on 12 April 2021).

Data Availability Statement: All reported results have been obtained during our research.

Acknowledgments: We are grateful to Lyudmila Vladimirovna Kuleshevich who is gone by now. We also appreciate reviewers for the valuable comments that helped to improve the manuscript.

Conflicts of Interest: We declare that this manuscript is original, has not been published before and is not currently being considered for publication elsewhere. The authors declare no conflict of interest.

Appendix A Sulfide Petrography

Several sulfide occurrence styles can be distinguished at the Leksa deposit based on mineral association, texture, and lithology of the host-rocks. We use the classification emphasizing the most important characteristics.

Pyrite dominates in massive and semi-massive ores of the Leksa deposit. Initially the ore consisted of large (up to 1 mm) and more isometric crystals of massive pyrite Figure A1B), sometimes with small chalcopyrite, sphalerite, and galena inclusions. This pyrite resulted from iron sulfide rapid massive precipitation from a high-temperature hydrothermal solution. The following metamorphism led to cleavage and partial recrystallization of primary pyrite. This resulted in the formation of a fine-grained texture composed of many different-sized, mainly xenomorphic, crystals (Figure A1C,D), sometimes containing a large amount of silicate inclusions (porous pyrite). This texture is well observed after sample etching using 70% nitric acid (HNO_3).

Pyrite precipitation textures and forms in poor disseminated ores and host-rocks are different. These ores consist of dispersed pyrite in the form of single crystals, microcrystalline aggregates of irregular shape, microspheres and subspherical formations, framboids (Figure A2). Pyrite is frequently confined to high-C rock segments. Pyrite crystallized from near the bottom or interstitial waters of sedimentary host-rocks.

Collomorphous forms of pyrite are found in carbonaceous sediments. They form irregular lenses, oval and ellipsoid globular aggregates with a clearly visible lamination that is sometimes concentric (Figure A3). Their matrix is represented by dendrite-like pyrite forming fine-grained structures of intimate intergrowths of iron sulfide thin acicular and bladed crystals with silicate minerals (quartz, chlorite, muscovite, graphite etc.). These intergrowths often have a radial fibrous or interwoven-fibrous texture, which possibly indicates that crystals grow fast in viscous, low-mobility glazer masses due to high crystallization rate of iron sulfide. According to XRD data collomorphous aggregates contain pyrite and marcasite. The further coalescence of dendrite-like crystals led to occurrence of reticulate (E,F) massive porous (C,D) textures.

The figure shows three different microstructures indicating the consecutive order of crystallization stages. Early pyrite (Figure A3E–G) consists of submillimeter acicular or box-like crystals and agglomerates of pyrite 2–20 μm in size with an abundant silicate inclusion (dendrite-like pyrite). Early pyrite is replaced with massive pyrite (Figure A3B–D) containing only small silicate inclusions. Massive pyrite is composed of microcrystals of early pyrite cemented by a later pyrite filling the gaps and replacing silicate minerals. Late-stage pyrite is found as idiomorphic grains without inclusions filling the cracks; it overgrows in the form of a crown collomorphous aggregate associated with quartz.

In situ analyses revealed strongly heterogenous $\delta^{34}S$ values, ranging from −6.7‰ to +27.5‰ in concentrically laminated pyrite grains. The $\Delta^{33}S$ values mainly vary between −0.3‰ and +0.5‰. The exception is relatively large positive $\Delta^{33}S$ = +1.4‰ measured in the core of the concentrically laminated pyrite.

Euhedral pyrite crystals around the concentrically laminated pyrite are relatively homogeneous in $\delta^{34}S$ and $\Delta^{33}S$ values, ranging from +4.6‰ to +7.0‰ and from +1.55‰ to +1.93‰, respectively.

Carbonaceous shales contain spheroids (vesicles) of pyrite (Figure A5). Morphological analysis of their walls shows that vesicles are fractal. Large spheres 10–20 mm in diameter

consist of multiple smaller vesicles (d = 1–2 mm) composed of even smaller spheres. Moreover, certain cases allow the formation of a tubular structure of large sphere walls (Figure A5E,F). In some cases, it is possible to identify a thin carbon film both on the internal and external walls of a sphere or its fragment (Figure A5F). Findings of spheroid microstructures in the Archean deposits are subject to a fierce debate.

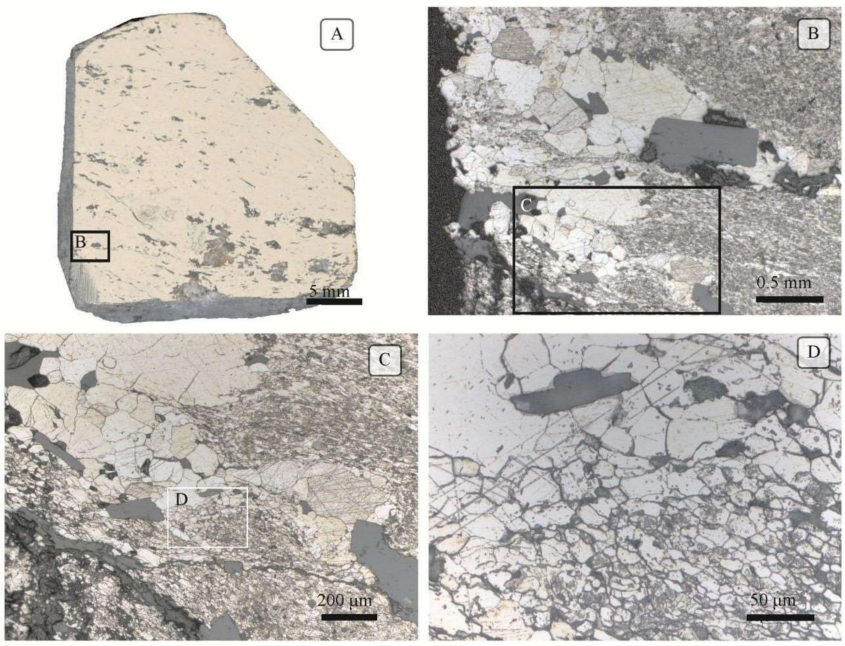

Figure A1. Massive pyrite ore, polished section, reflected light microscopy, sample H1-38,9: (**A**) Massive sulfide ore image; (**B**–**D**) relicts of primary pyrite crystals and their relationship with silicate minerals and fine-grained pyrite. Please note that fine-grained mass bears traces of metamorphic cleavage.

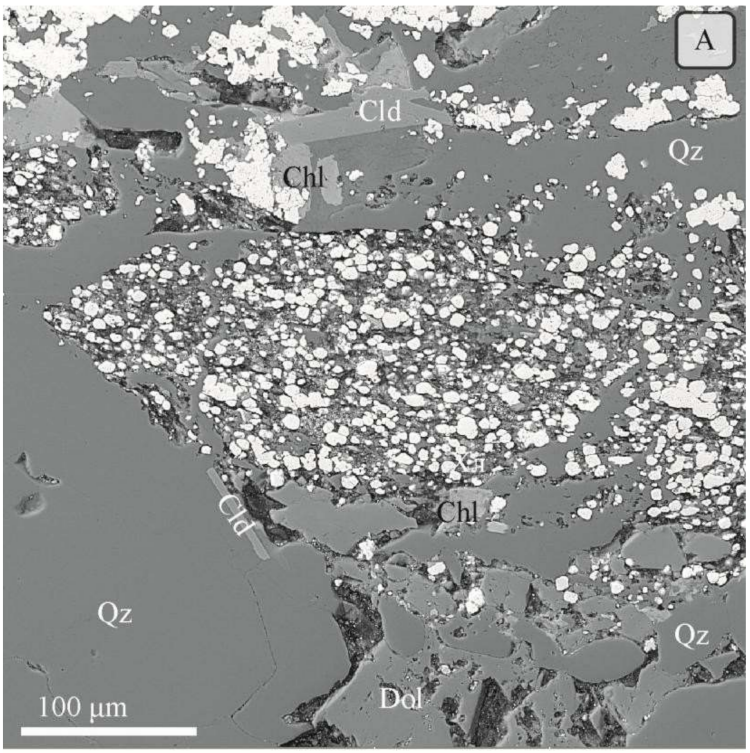

Figure A2. *Cont*.

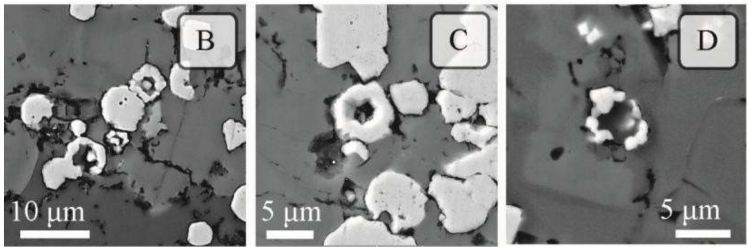

Figure A2. BSE image of finely dispersed precipitations of globular and microcrystalline pyrite in quartz–carbonate matrix of the host-rock (polished section, sample H3-56): (**A**) general view of finely dispersed pyrite accumulation; (**B**–**D**) typical shapes of microcrystals. They are represented by both separate euhedral crystals (**B**,**C**) and their isometric (**C**) and subspherical (**B**–**D**) intergrowths consisting of small (0.5–1.0 μm) vesicles.

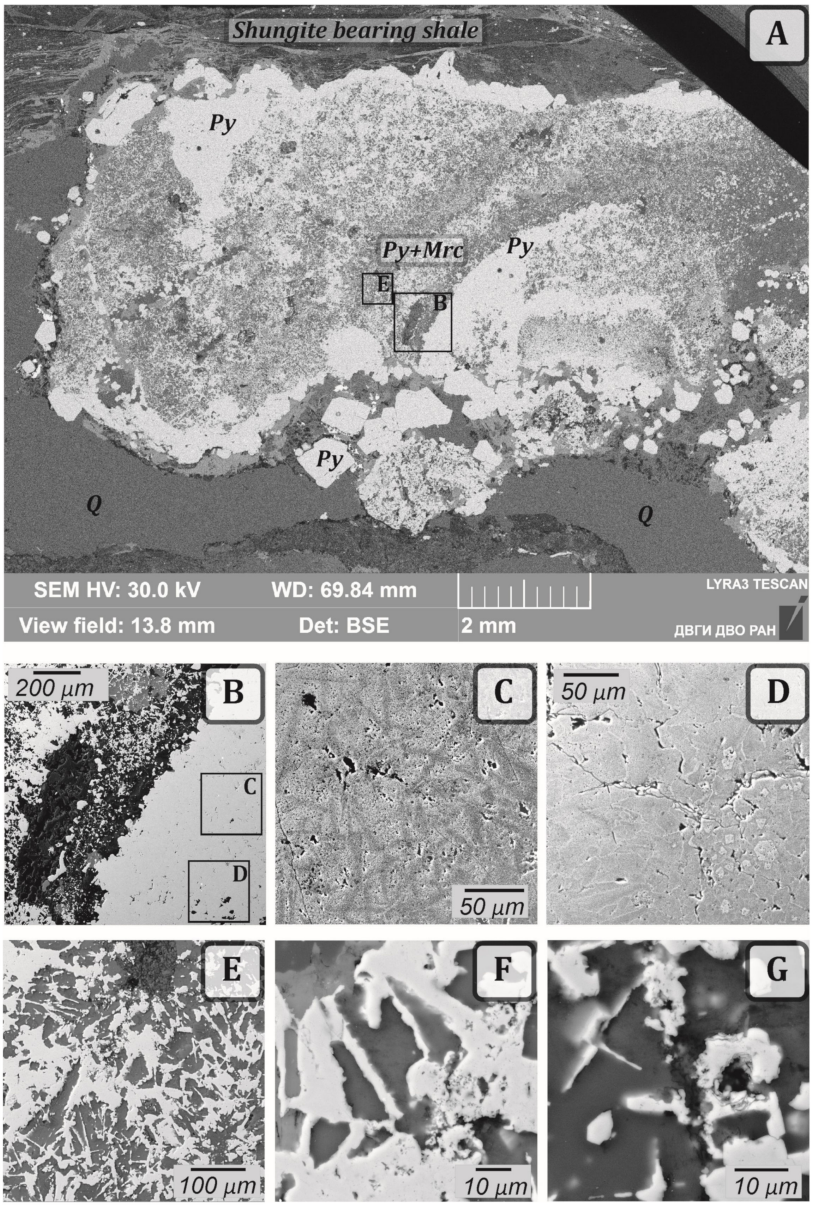

Figure A3. Collomorphous pyrite, BSE image (**A**–**E**). Laminated aggregate bordered with carbonaceous shale. It should be noted that parts (**F**,**G**) are outside of part (**A**).

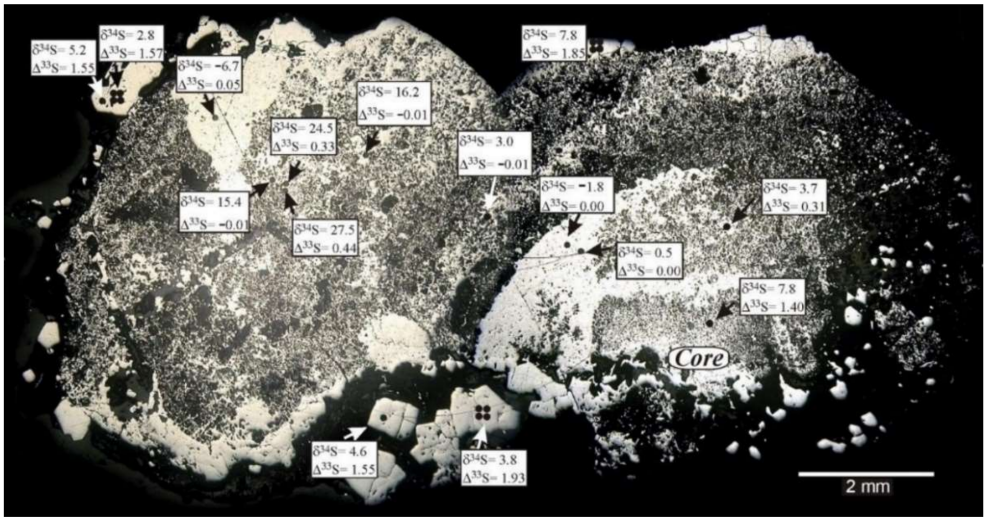

Figure A4. Reflected light microscopy image of the concentrically laminated pyrite grains surrounded by euhedral pyrite crystals. Note that the sample is the same as in Figure A3A. Also shown are ablation pits for in situ sulfur isotope analysis of $\delta^{34}S$ and $\Delta^{33}S$.

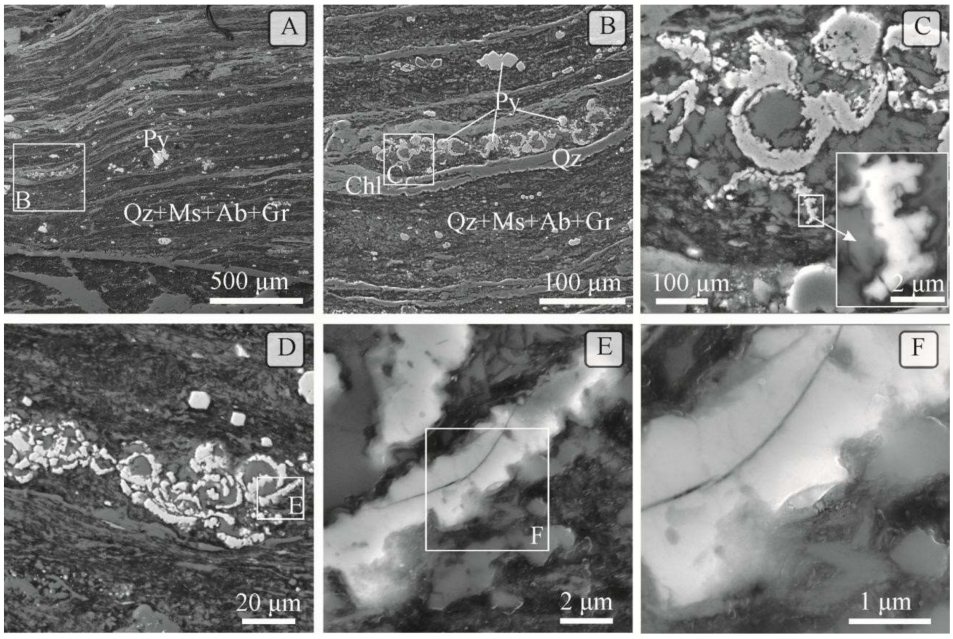

Figure A5. BSE image of pyrite microspheres (vesicular microstructures) and their debris in a carbonaceous shale, polished section, sample H1-75, the Leksa deposit: (**A**,**B**) general view of a shale composed of thin layers of quartz, chlorite (chamosite), muscovite, carbonaceous matter and pyrite microsphere accumulations in it. Microspheres and their debris have a complex structure, consisting of individual equant microcrystals (**C**,**D**), and in some cases it can be assumed that their walls are tubular (**E**,**F**).

Some scientists consider them to be traces of microorganism activity (see, for example, ref. [110] and references therein); others interpret them as pyritized and silicified fragments of vesicular volcanic glass ([111]). In the present case it is difficult to suggest that these characteristics are typical of abiotic.

Table A1. Isotopic data for pyrite from sedimentary rocks of the Leksa deposit.

Sample (Drill Core/Depth)	$\delta^{34}S$ (‰)	$\Delta^{33}S$ (‰)	$\Delta^{36}S$ (‰)	Pyrite Types
H1/50.7	−1.3	0.03		Euhedral crystal disseminated in rocks
H1/50.7	−0.1	−0.04		Euhedral crystal disseminated in rocks
H1/50.7	−0.9	−0.02		Euhedral crystal disseminated in rocks
H1/50.7	−1.2	0.03		Euhedral crystal disseminated in rocks
H1/50.7	5.4	0.04		Euhedral crystal disseminated in rocks
H1/54.6	13.4	0.02		Euhedral crystal disseminated in rocks
H1/54.6	13.9	0.34		Euhedral crystal disseminated in rocks
H1/54.6	13.5	−0.02		Euhedral crystal disseminated in rocks
H1/54.6	−3.2	0.00		Euhedral crystal disseminated in rocks
H1/54.6	−2.9	−0.05		Euhedral crystal disseminated in rocks
H1/63	−1.0	0.00		Euhedral crystal disseminated in rocks
H1/75	−4.8	0.84		Euhedral crystal disseminated in rocks
H1/75	−4.2	−0.38		Euhedral crystal disseminated in rocks
H1/75	−7.0	0.23		Euhedral crystal disseminated in rocks
H1/75	−1.0	−0.51		Euhedral crystal disseminated in rocks
H2/24.0	31.9	−0.18		Euhedral crystal disseminated in rocks
H2/24.0	32.7	−0.16		Euhedral crystal disseminated in rocks
H2/61.5	2.6	−0.01		Euhedral crystal disseminated in rocks
H2/61.5	2.3	0.04		Euhedral crystal disseminated in rocks
H2/61.5	−5.1	0.05		Euhedral crystal disseminated in rocks
H2/61.5	2.4	−0.02		Euhedral crystal disseminated in rocks
H2/61.5	2.2	0.02		Euhedral crystal disseminated in rocks
H3/56.0	13.8	1.48		Euhedral crystal disseminated in rocks
H3/56.0	12.6	1.28		Euhedral crystal disseminated in rocks
H3/56.0	7.6	0.25		Euhedral crystal disseminated in rocks
H3/56.0	11.5	0.40		Euhedral crystal disseminated in rocks
H3/56.0	13.8	0.12		Euhedral crystal disseminated in rocks
H3/56.0	11.6	0.28		Euhedral crystal disseminated in rocks
H3/56.0	12.1	0.32		Euhedral crystal disseminated in rocks
H3/56.0	10.2	0.28		Euhedral crystal disseminated in rocks
H3/56.0	12.0	0.35		Euhedral crystal disseminated in rocks
H3/56.0	11.9	0.28		Euhedral crystal disseminated in rocks
H3/56.0	10.3	0.41		Euhedral crystal disseminated in rocks
H3/56.0	5.4	0.10		Euhedral crystal disseminated in rocks
H3/56.0	16.9	0.67		Euhedral crystal disseminated in rocks
H3/56.0	12.2	0.42		Euhedral crystal disseminated in rocks

Table A1. *Cont.*

Sample (Drill Core/Depth)	$\delta^{34}S$ (‰)	$\Delta^{33}S$ (‰)	$\Delta^{36}S$ (‰)	Pyrite Types
H1/75	9.9	1.65		Euhedral, observed as ring-shaped aggregates
H1/75	11.0	2.65		Euhedral, observed as ring-shaped aggregates
H1/75	3.7	1.76	−1.3	Euhedral, observed as ring-shaped aggregates
H1/75	2.8	1.57	−2.0	Euhedral, observed as ring-shaped aggregates
H1/75	3.8	1.93	−2.4	Euhedral, observed as ring-shaped aggregates
H1/75	3.8	1.85	−2.5	Euhedral, observed as ring-shaped aggregates
H1/75	6.1	1.95		Euhedral crystal, overgrowth around colloform grains
H1/75	6.3	2.20		Euhedral crystal, overgrowth around colloform grains
H1/75	5.2	1.55		Euhedral crystal, overgrowth around colloform grains
H1/75	4.6	1.55		Euhedral crystal, overgrowth around colloform grains
H1/75	5.3	1.93		Euhedral crystal, overgrowth around colloform grains
H1/75	5.2	1.96		Euhedral crystal, overgrowth around colloform grains
H1/75	5.1	1.85		Euhedral crystal, overgrowth around colloform grains
H1/75	7.0	2.64		Euhedral crystal, overgrowth around colloform grains
H1/75	5.7	2.06		Euhedral crystal, overgrowth around colloform grains
H1/75	5.9	2.02		Euhedral crystal, overgrowth around colloform grains
H1/75	7.8	1.40		Colloform grains_1, core
H1/75	3.7	0.31		Colloform grains_1, concentric layer
H1/75	0.5	0.00		Colloform grains_1, concentric layer
H1/75	−1.8	0.00		Colloform grains_1, concentric layer
H1/75	3.0	−0.01		Colloform grains_1, concentric layer
H1/75	16.2	−0.01		Colloform grains_1, concentric layer
H1/75	27.5	0.44		Colloform grains_1, concentric layer
H1/75	24.5	0.33		Colloform grains_1, concentric layer
H1/75	15.4	−0.01		Colloform grains_1, concentric layer
H1/75	−6.7	0.05		Colloform grains_1, concentric layer
H1/75	−9.5	0.13		Colloform grains_2, non-laminated
H1/75	−9.8	0.22		Colloform grains_2, non-laminated
H1/75	−10.2	0.11		Colloform grains_2, non-laminated
H1/75	7.0	0.08		Colloform grains_3, non-laminated
H1/75	1.6	−0.30		Colloform grains_3, non-laminated
H1/75	−6.6	−0.27		Colloform grains_3, non-laminated

Table A1. *Cont.*

Sample (Drill Core/Depth)	$\delta^{34}S$ (‰)	$\Delta^{33}S$ (‰)	$\Delta^{36}S$ (‰)	Pyrite Types
H3/56.0	5.7	0.17		Colloform grains_4, core
H3/56.0	8.5	0.23		Colloform grains_4, concentric layer
H3/56.0	10.6	0.48		Colloform grains_4, concentric layer
H3/56.0	10.1	0.49		Colloform grains_4, concentric layer
H3/56.0	11.9	0.45		Colloform grains_4, concentric layer

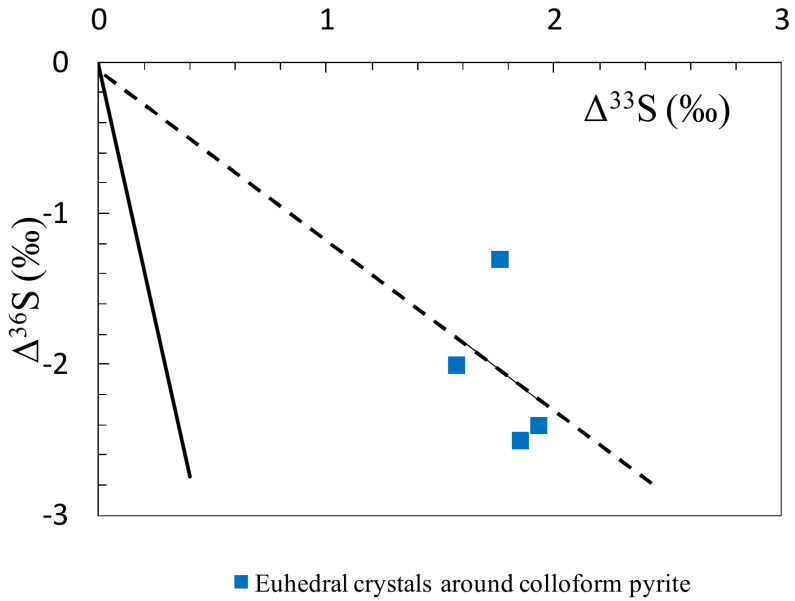

Figure A6. Plot of $\Delta^{33}S$ versus $\Delta^{36}S$ for the euhedral pyrite crystals from the sample, showing in Figure A4. The dashed line on the plot is a linear fit to data with a slope of −1.15. Also shown is the solid line with a slope of −6.85 for mass-dependent sulfur isotope fractionation in Phanerozoic samples, reported in [31]. Note that our data cannot be associated with microbial mass-dependent sulfur isotope fractionation.

References

1. Jørgensen, B.B.; Isaksen, M.F.; Jannasch, H.W. Bacterial sulfate reduction above 100° C in deep-sea hydrothermal vent sediments. *Science* **1992**, *258*, 1756–1757. [CrossRef]
2. Jørgensen, B.B.; Findlay, A.J.; Pellerin, A. The Biogeochemical sulfur cycle of marine sediments. *Front. Microbiol.* **2019**, *10*, 849. [CrossRef]
3. Hofmann, H.J.; Grey, K.; Hickman, A.H.; Thorpe, R.I. Origin of 3.45 Ga coniform stromatolites in Warrawoona Group, Western Australia. *Geol. Soc. Am. Bull.* **1999**, *111*, 1256–1262. [CrossRef]
4. Philippot, P.; Van Zuilen, M.; Lepot, K.; Thomazo, C.; Farquhar, J.; Van Kranendonk, M.J. Early Archaean microorganisms preferred elemental sulfur, not sulfate. *Science* **2007**, *317*, 1534–1537. [CrossRef] [PubMed]
5. Philippot, P.; Van Zuilen, M.; Rollion-Bard, C. Variations in atmospheric sulphur chemistry on early Earth linked to volcanic activity. *Nat. Geosci.* **2012**, *5*, 668–674. [CrossRef]
6. Ueno, Y.; Ono, S.; Rumble, D.; Maruyama, S. Quadruple sulfur isotope analysis of ca. 3.5 Ga Dresser Formation: New evidence for microbial sulfate reduction in the early Archean. *Geochim. Cosmochim. Acta* **2008**, *72*, 5675–5691. [CrossRef]
7. Shen, Y.; Farquhar, J.; Masterson, A.; Kaufman, A.J.; Buick, R. Evaluating the role of microbial sulfate reduction in the early Archean using quadruple isotope systematics. *Earth Planet. Sci. Lett.* **2009**, *279*, 383–391. [CrossRef]
8. Wacey, D.; Noffke, N.; Cliff, J.; Barley, M.E.; Farquhar, J. Micro-scale quadruple sulfur isotope analysis of pyrite from the ~3480 Ma Dresser Formation: New insights into sulfur cycling on the early Earth. *Precambrian Res.* **2015**, *258*, 24–35. [CrossRef]

9. Baumgartner, R.J.; Caruso, S.; Fiorentini, M.L.; van Kranendonk, M.J.; Martin, L.; Jeon, H.; Pagès, A.; Wacey, D. Sulfidization of 3.48 billion-year-old stromatolites of the Dresser Formation, Pilbara Craton: Constraints from in-situ sulfur isotope analysis of pyrite. *Chem. Geol.* **2020**, *538*, 119488. [CrossRef]
10. Roerdink, D.L.; Mason, P.R.D.; Whitehouse, M.J.; Reimer, T. High-resolution quadruple sulfur isotope analyses of 3.2 Ga pyrite from the Barberton Greenstone Belt in South Africa reveal distinct environmental controls on sulfide isotopic arrays. *Geochim. Cosmochim. Acta* **2013**, *117*, 203–215. [CrossRef]
11. Montinaro, A.; Strauss, H.; Mason, P.R.D.; Roerdink, D.; Münker, C.; Schwarz-Schampera, U.; Arndt, N.T.; Farquhar, J.; Beukes, N.J.; Gutzmer, J.; et al. Paleoarchean sulfur cycling: Multiple sulfur isotope constraints from the Barberton Greenstone Belt, South Africa. *Precambrian Res.* **2015**, *267*, 311–322. [CrossRef]
12. Nabhan, S.; Marin-Carbonne, J.; Mason, P.R.D.; Heubeck, C. In situ S-isotope compositions of sulfate and sulfide from the 3.2 Ga Moodies Group, South Africa: A record of oxidative sulfur cycling. *Geobiology* **2020**, *18*, 426–444. [CrossRef]
13. Canfield, D.E. Biogeochemistry of sulfur isotopes. *Rev. Miner. Geochem.* **2001**, *43*, 607–636. [CrossRef]
14. Shen, Y.; Buick, R.; Canfield, D.E. Isotopic evidence for microbial sulphate reduction in the early Archaean era. *Nature* **2001**, *410*, 77–81. [CrossRef]
15. Liu, L.; Ireland, T.R.; Holden, P. SHRIMP 4-S isotope systematics of two pyrite generations in the 3.49 Ga Dresser Formation. *Geochem. Perspect. Lett.* **2021**, *17*, 45–49. [CrossRef]
16. Kaufman, A.J.; Johnston, D.T.; Farquhar, J.; Masterson, A.L.; Lyons, T.W.; Bates, S.; Anbar, A.D.; Arnold, G.L.; Garvin, J.; Buick, R. Late Archean biospheric oxygenation and atmospheric evolution. *Science* **2007**, *317*, 1900–1903. Available online: https://www.jstor.org/stable/20048474 (accessed on 28 September 2007). [CrossRef] [PubMed]
17. Ono, S.; Beukes, N.; Rumble, D. Origin of two distinct multiple-sulfur isotope compositions of pyrite in the 2.5 Ga Klein Naute Formation, Griqualand West Basin, South Africa. *Precambrian Res.* **2009**, *169*, 48–57. [CrossRef]
18. Ono, S.; Kaufman, A.J.; Farquhar, J. Lithofacies control on multiple-sulfur isotope records and Neoarchean sulfur cycles. *Precambrian Res.* **2009**, *169*, 58–67. [CrossRef]
19. Zerkle, A.L.; Claire, M.W.; Domagal-Goldman, S.D.; Farquhar, J.; Poulton, S.W. A bistable organic-rich atmosphere on the Neoarchaean Earth. *Nat. Geosci.* **2012**, *5*, 359–363. [CrossRef]
20. Farquhar, J.; Cliff, J.; Zerkle, A.L.; Kamyshny, A.; Poulton, S.W.; Claire, M.; Adams, D.; Harms, B. Pathways for Neoarchean pyrite formation constrained by mass-independent sulfur isotopes. *Proc. Natl. Acad. Sci. USA* **2013**, *110*, 17638–17643. [CrossRef]
21. Zhelezinskaia, I.; Kaufman, A.J.; Farquhar, J.; Cliff, J. Large sulfur isotope fractionations associated with Neoarchean microbial sulfate reduction. *Science* **2014**, *346*, 742–744. [CrossRef] [PubMed]
22. Farquhar, J.; Peters, M.; Johnston, D.T.; Strauss, H.; Masterson, A.; Wiechert, U.; Kaufman, A.J. Isotopic evidence for Mesoarchaean anoxia and changing atmospheric sulphur chemistry. *Nature* **2007**, *449*, 706–709. [CrossRef] [PubMed]
23. Guy, B.M.; Ono, S.; Gutzmer, J.; Kaufman, A.J.; Lin, Y.; Fogel, M.L.; Beukes, N.J. A multiple sulfur and organic carbon isotope record from non-conglomeratic sedimentary rocks of the Mesoarchean Witwatersrand Supergroup, South Africa. *Precambrian Res.* **2012**, *216–219*, 208–231. [CrossRef]
24. Ono, S.; Beukes, N.J.; Rumble, D.; Fogel, M.L. Early evolution of atmospheric oxygen from multiple-sulfur and carbon isotope records of the 2.9 Ga Mozaan Group of the Pongola Supergroup, Southern Africa. *S. Afr. J. Geol.* **2006**, *109*, 97–108. [CrossRef]
25. Strauss, H. Sulphur isotopes and the early Archaean sulphur cycle. *Precambrian Res.* **2003**, *126*, 349–361. [CrossRef]
26. Farquhar, J.; Bao, H.; Thiemens, M. Atmospheric influence of Earth's earliest sulphur cycle. *Science* **2000**, *289*, 756–758. [CrossRef]
27. Johnston, D. Multiple sulfur isotopes and the evolution of Earth's surface sulfurcycle. *Earth-Sci. Rev.* **2011**, *106*, 161–183. [CrossRef]
28. Farquhar, J.; Savarino, J.; Airieau, S.; Thiemens, M.H. Observation of wavelength-sensitive mass-independent sulfur isotope effects during SO_2 photolysis: Implications for the early atmosphere. *J. Geophys. Res.* **2001**, *106*, 32829–32839. [CrossRef]
29. Pavlov, A.A.; Kasting, J.F. Mass-independent fractionation of sulphur isotopesin Archaean sediments: Strong evidence for an anoxic Archaean atmosphere. *Astrobiology* **2002**, *2*, 27–41. [CrossRef]
30. Ono, S.; Eigenbrode, J.L.; Pavlov, A.A.; Kharecha, P.; Ruble, D.; Kasting, J.F.; Freeman, K.H. New insights into Archean sulfur cycle from mass-independent sulfurisotope records from the Hamersley Basin, Australia. *Earth Planet. Sci. Lett.* **2003**, *213*, 15–30. [CrossRef]
31. Ono, S.; Wing, B.; Johnston, D.; Farquhar, J.; Rumble, D. Mass-dependent fractionation of quadruple stable sulfur isotope system as a new tracer of sulfur biogeochemical cycles. *Geochim. Cosmochim. Acta* **2006**, *70*, 2238–2252. [CrossRef]
32. Glebovitskii, V.A. *The Early Precambrian of the Baltic Shield*; Nauka: St. Petersburg, Russia, 2005. (In Russain)
33. Hölttä, P.; Heilimo, E.; Huhma, H.; Kontinen, A.; Mertanen, S.; Mikkola, P.; Paavola, J.; Peltonen, P.; Semprich, J.; Slabunov, A.; et al. The Archaean of the Karelia Province in Finland. *Geol. Surv. Finl. Spec. Pap.* **2012**, *54*, 21–73.
34. Kulikov, V.S.; Svetov, S.A.; Slabunov, A.I.; Kulikova, V.V.; Polin, A.K.; Golubev, A.I.; Gorkovets, V.Y.; Ivashchenko, V.I.; Gogolev, M.A. Geological map of Southeastern Fennoscandia (scale 1:750 000): A new approach to map compilation. *Trans. KarRC RAS.* **2017**, *2*, 3–41. [CrossRef]
35. Slabunov, A.I.; Lobach-Zhuchenko, S.B.; Bibikova, E.V.; Sorjonen-Ward, P.; Balagansky, V.V.; Volodichev, O.I.; Shchipansky, A.A.; Svetov, S.A.; Chekulaev, V.P.; Arestova, N.A.; et al. The Archaean Nucleus of the Baltic/Fennoscandian Shield. In *European Lithosphere Dynamics: Geological Society of London, Memoir*; Gee, D.G., Stephenson, R.A., Eds.; European Lithosphere Dynamics Geological Society: London, UK, 2006; Volume 32, pp. 627–644.

36. Slabunov, A.I.; Nesterova, N.S.; Egorov, A.V.; Kuleshevich, L.V.; Kevlich, V.I. Age of the Archean strata with banded iron formation in the Kostomuksha Greenstone Belt, Karelian Craton, Fennoscandian Shield: Constraints on the geochemistry and geochronology of zircons. *Geochem. Int.* **2021**, *59*, 341–356. [CrossRef]
37. Hölttä, P.; Heilimo, E.; Huhma, H.; Kontinen, A.; Mertanen, S.; Mikkola, P.; Paavola, J.; Peltonen, P.; Semprich, J.; Slabunov, A.; et al. The Archaean Karelia and Belomorian Provinces, Fennoscandian Shield. In *Evolution of Archean Crust and Early Life. Modern Approaches in Solid Earth Sciences*; Dilek, Y., Furnes, H., Eds.; Springer: Berlin/Heidelberg, Germany, 2014; pp. 55–102. [CrossRef]
38. Lobach-Zhuchenko, S.B.; Chekulaev, V.P.; Arestova, N.A.; Levskii, L.K.; Kovalenko, A.V. Archaean terranes in Karelia: Geological and isotopic–geochemical evidence. *Geotectonics* **2000**, *34*, 452–466.
39. Puchtel, I.S.; Hofmann, A.W.; Amelin, Y.u.V.; Garbe-Schönberg, C.-D.; Samsonov, A.V.; Shchipansky, A.A. Combined mantle plume-island arc model for the formation of the 2.9 ga Sumozero-Kenozero greenstone belt, se baltic shield: Isotope and trace element constraints. *Geochim. Cosmochim. Acta* **1999**, *63*, 3579–3595. [CrossRef]
40. Kuleshevich, L.V. *Metamorphism and Ore Potential of Archean Greenstone Belts from the Southeastern Margin of the Baltic Shield*; Karelian Scientific Center: Petrozavodsk, Russia, 1992. (In Russian)
41. Kuleshevich, L.V.; Furman, V.N.; Fedyuk, Z.N. Promises for gold mineralization in the Kamenoozero structure of the Sumozero-Kenozero greenstone belt. *Geol. Useful Miner. Karelia.* **2005**, *8*, 50–67. (In Russian)
42. Hölttä, P.; Heilimo, E.; Huhma, H.; Kontinen, A.; Lauri, L.; Slabunov, A. Paleoarchean rocks in the Fennoscandian Shield (Chapter 32). In *Earth's Oldest Rocks*, 2nd ed.; Van Kranendonk, M.J., Bennett, V.C., Hoffmann, J.E., Eds.; Elsevier: Amsterdam, The Netherlands, 2019; pp. 819–836.
43. Vysotskii, S.V.; Khanchuk, A.I.; Kuleshevich, L.V.; Ignatiev, A.V.; Slabunov, A.I.; Velivetskaya, T.A. The Multi-isotope composition of sulfur in sulfides and microfossils of the Mesoarchean Leksa pyrite ore occurrence of the Karelian Craton: New data on abiogenic and biogenic effects on the formation of ancient ores. *Dokl. Earth Sci.* **2019**, *485*, 409–412. [CrossRef]
44. Vysotskiy, S.V.; Slabunov, A.I.; Ignatiev, A.V.; Kuleshevich, L.V.; Velivetskaya, T.A. Multiple sulfur isotopes from Mesoarchean volcano-sedimentary massive sulfide deposits of the Karelian Craton: Significance for determining sulfur sources, biogeochemical processes and the genesis of deposits. *Russ. Geol. Geophys.* **2022**. [CrossRef]
45. Kuleshevich, L.V.; Belashev, B.Z. Pyrite mineralization in East Karelia (experience in studying the composition and electrophysical properties of pyrites). *Geol. Miner. Karelia* **1998**, *1*, 57–72. (In Russian)
46. Galley, A.G.; Hannington, M.; Jonasson, I. Volcanogenic massive sulphide deposits. In *Mineral Deposits of Canada—A Synthesis of Major Deposit-Types, District Metallogeny, the Evolution of Geological Provinces, and Exploration Methods*; Goodfellow, W.D., Ed.; Special Publication 5; Geological Association of Canada, Mineral Deposits Division: Saint John, NB, Canada, 2007; pp. 141–161.
47. Hannington, M.D.; Bleeker, W.; Kjarsgaard, I. Sulfide mineralogy, geochemistry, and ore genesis of the Kidd Creek deposit—Part I. North, central, and south orebodies. In *The Giant Kidd Creek Volcanogenic Massive Sulfide Deposit, Western Abitibi Subprovince, Canada*; Hannington, M.D., Barrie, C.T., Eds.; Economic Geology Monograph Series; Geo Science World: McLean, VA, USA, 1999; Volume 10, pp. 163–224. [CrossRef]
48. Goodfellow, W.D.; McCutcheon, S.R. Geologic and genetic attributes of volcanic sediment-hosted massive sulfide deposits of the Bathurst mining camp, New Brunswick—A synthesis. In *Massive Sulfide Deposits of the Bathurst Mining Camp, New Brunswick, and Northern Maine*; Goodfellow, W.D., McCutcheon, S.R., Peter, J.M., Eds.; Economic Geology Monograph Series; Geo Science World: McLean, VA, USA, 2003; Volume 11, pp. 245–301.
49. Barrie, C.T.; Hannington, M.D. Classification of volcanic-associated massive sulfide deposits based on host-rock composition. In *Volcanic-Associated Massive Sulfide Deposits: Progresses and Examples in Modern and Ancient Settings*; Barrie, C.T., Hannington, M.D., Eds.; Reviews in Economic Geology; Geo Science World: McLean, VA, USA, 1999; Volume 8, pp. 1–11. [CrossRef]
50. Franklin, J.M.; Gibson, H.L.; Jonasson, I.R.; Galley, A.G. Volcanogenic massive sulfide deposits. In *One Hundredth Anniversary Volume*; Hedenquist, J.W., Thompson, J.F.H., Goldfarb, R.J., Richards, J.P., Eds.; Geo Science World: McLean, VA, USA, 2005; pp. 523–560. [CrossRef]
51. Hannington, M.D.; de Ronde, C.E.; Petersen, S. *Sea-Floor Tectonics and Submarine Hydrothermal Systems. Economic Geology 100th Anniversary Volume, 1905–2005: Littleton, Colo*; Hedenquist, J.W., Thompson, J.F.H., Goldfarb, R.J., Richards, J.P., Eds.; Geo Science World: McLean, VA, USA, 2005; pp. 111–141. [CrossRef]
52. Ignatiev, A.V.; Velivetskaya, T.A.; Budnitskiy, S.Y.; Yakovenko, V.V.; Vysotskiy, S.V.; Levitskii, V.I. Precision analysis of multisulfur isotopes in sulfides by femtosecond laser ablation GC-IRMS at high spatial resolution. *Chem. Geol.* **2018**, *493*, 316–326. [CrossRef]
53. Velivetskaya, T.A.; Ignatiev, A.V.; Yakovenko, V.V.; Vysotskiy, S.V. An improved femtosecond laser-ablation fluorination method for measurements of sulfur isotopic anomalies (Δ33S and Δ36S) in sulfides with high precision. *Rapid Commun. Mass Spectrom.* **2019**, *33*, 1722–1729. [CrossRef] [PubMed]
54. Farquhar, J.; Savarino, J.; Jackson, T.L.; Thiemens, M.H. Evidence of atmospheric sulphur in the martian regolith from sulphur isotopes in meteorites. *Nature* **2000**, *404*, 50–52. [CrossRef] [PubMed]
55. Berner, R.A. Sedimentary pyrite formation. *Am. J. Sci.* **1970**, *268*, 1–23. [CrossRef]
56. Rickard, D.T. Kinetics of pyrite formation by the H2S oxidation of iron (II) monosulfide in aqueous solutions between 25 and 125°C: The rate equation. *Geochim. Cosmochim. Acta* **1997**, *61*, 115–134. [CrossRef]
57. Rickard, D.; Luther, G.W., III. Kinetics of pyrite formation by the H2S oxidation of iron (II) monosulfide in aqueous solutions between 25 and 125°C: The mechanism. *Geochim. Cosmochim. Acta* **1997**, *61*, 135–147. [CrossRef]

58. Masterson, A.L.; Farquhar, J.; Wing, B.A. Sulfur mass-independent fractionation patterns in the broadband UV photolysis of sulfur dioxide: Pressure and third body effects. *Earth Planet Sci. Lett.* **2011**, *306*, 253–260. [CrossRef]
59. Whitehill, A.R.; Ono, S. Excitation band dependence of sulfur isotope mass-independent fractionation during photochemistry of sulfur dioxide using broadband light sources. *Geochim. Cosmochim. Acta* **2012**, *94*, 238–253. [CrossRef]
60. Ono, S.; Whitehill, A.R.; Lyons, J.R. Contribution of isotopologue self-shielding to sulfur mass-independent fractionation during sulfur dioxide photolysis. *J. Geophys. Res. Atmospheres* **2013**, *118*, 2444–2454. [CrossRef]
61. Whitehill, A.R.; Xie, C.; Hu, X.; Xie, D.; Guo, H.; Ono, S. Vibronic origin of sulfur mass-independent isotope effect in photoexcitation of SO_2 and the implications to the early earth's atmosphere. *Proc. Natl. Acad. Sci. USA* **2013**, *110*, 17697–17702. [CrossRef]
62. Endo, Y.; Ueno, Y.; Aoyama, S.; Danielache, S.O. Sulfur isotope fractionation by broadband UV radiation to optically thin SO_2 under reducing atmosphere. *Earth Planet Sci. Lett.* **2016**, *453*, 9–22.
63. Endo, Y.; Danielache, S.O.; Ueno, Y. Total pressure dependence of sulfur mass-independent fractionation by SO_2 photolysis. *Geophys. Res. Lett.* **2019**, *46*, 483–491. [CrossRef]
64. Ignatiev, A.V.; Velivetskaya, T.A.; Yakovenko, V.V. Effect of mass-independent isotope fractionation of sulfur ($\Delta^{33}S$ and $\Delta^{36}S$) during SO_2 photolysis in experiments with a broadband light source. *Geochem Int.* **2019**, *57*, 751–760. [CrossRef]
65. Velivetskaya, T.A.; Ignatiev, A.V.; Yakovenko, V.V. Mass-independent sulfur isotope fractionation in the photochemical SO_2 processes under the UV radiation of different wave length. *Geochem Int.* **2020**, *58*, 1228–1238. [CrossRef]
66. Thode, H.; Kleerekoper, H.; McElcheran, D. Isotope fractionation in the bacterial reduction of sulphate. *Research* **1951**, *4*, 581–582.
67. Kaplan, I.R.; Rafter, T.A. Fractionation of stable isotopes of sulfur by Thiobacilli. *Science* **1958**, *127*, 517–518. [CrossRef]
68. Kaplan, I.R.; Rittenberg, S.C. Microbiological fractionation of sulphur isotopes. *Microbiology* **1964**, *34*, 195–212. [CrossRef]
69. Kemp, A.L.W.; Thode, H.G. The mechanism of the bacterial reduction of sulphate and of sulphite from isotope fractionation studies. *Geochim. Cosmochim. Acta* **1968**, *32*, 71–91. [CrossRef]
70. Sim, M.S.; Bosak, T.; Ono, S. Large sulfur isotope fractionation does not require disproportionation. *Science* **2011**, *333*, 74–77. [CrossRef]
71. Drake, H.; Tullborg, E.-L.; Whitehouse, M.; Sandberg, B.; Blomfeldt, T.; Åström, M.E. Extreme fractionation and micro-scale variation of sulphur isotopes during bacterial sulphate reduction in deep groundwater systems. *Geochim. Cosmochim. Acta* **2015**, *161*, 1–18. [CrossRef]
72. Drake, H.; Whitehouse, M.J.; Heim, C.; Reiners, P.W.; Tillberg, M.; Hogmalm, K.J.; Dopson, M.; Broman, C.; Åström, M.E. Unprecedented ^{34}S-enrichment of pyrite formed following microbial sulfate reduction in fractured crystalline rocks. *Geobiology* **2018**, *16*, 556–574. [CrossRef] [PubMed]
73. Cavalazzi, B.; Agangi, A.; Barbieri, R.; Franchi, F.; Gasparotto, G. The formation of low-temperature sedimentary pyrite and its relationship with biologically-induced processes. *Geol. Ore Depos.* **2014**, *56*, 395–408. [CrossRef]
74. Hallbauer, D.K.; Barton, J.M. The fossil gold placers of the Witwatersrand. *Gold Bull.* **1987**, *20*, 68–79. [CrossRef]
75. Frizzo, P.; Rampazzo, G.; Molinaroli, E. Authigenic iron sulphides in Recent sediments of the Venice Lagoon (northern Italy). *Eur. J. Miner.* **1991**, *3*, 603–612. [CrossRef]
76. Huang, F.; Gao, S.; Chen, L.; Su, L.; Li, Y.; Meng, L.; Liu, K.; Chai, C.; Qi, X. Micro-texture and in situ sulfur isotope of pyrite from the Baiyunpu Pb-Zn deposit in central Hunan, South China: Implications for the growth mechanism of colloform pyrite aggregates. *J. Asian Earth Sci.* **2020**, *193*, 104302. [CrossRef]
77. Agangi, A.; Hofmann, A.; Rollion-Bard, C.; Marin-Carbonne, J.; Cavalazzi, B.; Large, R.; Meffre, S. Gold accumulation in the Archaean Witwatersrand Basin, South Africa—evidence from concentrically laminated pyrite. *Earth Sci. Rev.* **2015**, *140*, 27–53. [CrossRef]
78. Canfield, D.E. Isotope fractionation by natural populations of sulfate-reducing bacteria. *Geochim. Cosmochim. Acta* **2001**, *65*, 1117–1124. [CrossRef]
79. Habicht, K.S.; Gade, M.; Thamdrup, B.; Berg, P.; Canfield, D.E. Calibration of sulfate levels in the Archean Ocean. *Science* **2002**, *298*, 2372–2374. [CrossRef] [PubMed]
80. Jamieson, J.W.; Wing, B.A.; Farquhar, J.; Hannington, M.D. Neoarchaean seawater sulphate concentrations from sulphur isotopes in massive sulphide ore. *Nat. Geosci.* **2013**, *6*, 61–64. [CrossRef]
81. Crowe, S.A.; Paris, G.; Katsev, S.; Jones, C.; Kim, S.-T.; Zerkle, A.L.; Nomosatryo, S.; Fowle, D.A.; Adkins, J.F.; Sessions, A.L.; et al. Sulfate was a trace constituent of Archean seawater. *Science* **2014**, *346*, 735–739. Available online: https://www.jstor.org/stable/24917791 (accessed on 7 November 2014). [CrossRef]
82. Canfield, D.E. The evolution of the Earth surface sulfur reservoir. *Am. J. Sci.* **2004**, *304*, 839–861. [CrossRef]
83. Ingvorsen, K.; Zehnder, A.J.B.; Jørgensen, B.B. Kinetics of sulfate and acetate uptake by Desulfobacter postgatei. *Appl. Environ. Microbiol.* **1984**, *47*, 403–408. [CrossRef] [PubMed]
84. Ono, S.; Eigenbrode, J.L.; Pavlov, A.A.; Kharecha, P.; Rumble, D.; Kasting, J.F.; Freeman, K.H. New insights into Archaean sulfur cycle from mass-independent sulfur isotope records from the Hamersley Basin, Australia. *Earth Planet Sci. Lett.* **2003**, *213*, 15–30. [CrossRef]
85. Cypionka, H.; Smock, A.M.; Bottcher, M.E. A combined pathway of sulfur compound disproportionation in Desulfovivrio desulfuricans. *FEMS Microbiol. Lett.* **1998**, *166*, 181–186. [CrossRef]

86. Canfield, D.E.; Thamdrup, B. The production of 34S depleted sulfide during bacterial disproportionation of elemental sulfur. *Science* **1994**, *266*, 1973–1975. [CrossRef] [PubMed]
87. Thamdrup, B.; Finster, K.; Hansen, J.W.; Bak, F. Bacterial disproportionation of elemental sulfur coupled to chemical reduction of iron or manganese. *Appl. Environ. Microbiol.* **1993**, *59*, 101–108. [CrossRef]
88. Canfield, D.E.; Thamdrup, B.; Fleischer, S. Isotope fractionation and metabolism by pure and enrichment cultures of elemental sulfur-disproportionating bacteria. *Limnol. Oceanogr.* **1998**, *43*, 253–264. [CrossRef]
89. Böttcher, M.E.; Thamdrup, B.; Vennemann, T.W. Oxygen and sulfur isotope fractionation during anaerobic bacterial disproportionation of elemental sulfur. *Geochim. Cosmochim. Acta* **2001**, *65*, 1601–1609. [CrossRef]
90. Böttcher, M.E.; Thamdrup, B. Anaerobic sulfide oxidation and stable isotope fractionation associated with bacterial sulfur disproportionation in the presence of MnO2. *Geochim. Cosmochim. Acta* **2001**, *65*, 1573–1581. [CrossRef]
91. Böttcher, M.E.; Thamdrup, B.; Gehre, M.; Theune, A. 34S/32S and 18O/16O fractionation during sulfur disproportionation by Desulfobulbus propionicus. *Geomicrobiol. J.* **2005**, *22*, 219–226. [CrossRef]
92. Johnston, D.T.; Farquhar, J.; Wing, B.A.; Kaufman, A.J.; Canfield, D.E.; Habicht, K.S. Multiple sulfur isotope fractionations in biological systems: A case study with sulfate reducers and sulfur disproportionators. *Am. J. Sci.* **2005**, *305*, 645–660. [CrossRef]
93. Canfield, D.E.; Teske, A. Late Proterozoic rise in atmospheric oxygen concentration inferred from phylogenetic and sulphur isotope studies. *Nature* **1996**, *382*, 127–132. [CrossRef] [PubMed]
94. Johnston, D.T.; Farquhar, J.; Canfield, D.E. Sulfur isotope insights into microbial sulfate reduction: When microbes meet models. *Geochim. Cosmochim. Acta* **2007**, *71*, 3929–3947. [CrossRef]
95. Farquhar, J.; Johnston, D.T.; Wing, B.A.; Habicht, K.S.; Canfield, D.E.; Airieau, S.; Thiemens, M.H. Multiple sulphur isotopic interpretations of biosynthetic pathways: Implications for biological signatures in the sulphur isotope record. *Geobiology* **2003**, *1*, 27–36. [CrossRef]
96. Farquhar, J.; Johnston, D.T.; Wing, B.A. Implications of conservation of mass effects on mass-dependent isotope fractionations: Influence of network structure on sulfur isotope phase space of dissimilatory sulfate reduction. *Geochim. Cosmochim. Acta* **2007**, *71*, 5862–5875. [CrossRef]
97. Ye, Y.T.; Wu, C.D.; Zhai, L.N.; An, Z.Z. Pyrite morphology and episodic euxinia of the Ediacaran Doushantuo Formation in South China. *Sci. China Inf. Sci.* **2017**, *60*, 102–113. [CrossRef]
98. Liu, Z.; Chen, D.; Zhang, J.; Lü, X.; Wang, Z.; Liao, W.; Shi, X.; Tang, J.; Xie, G. Pyrite morphology as an indicator of paleoredox conditions and shale gas content of the longmaxi and wufeng shales in the Middle Yangtze Area, South China. *Minerals* **2019**, *7*, 428. [CrossRef]
99. Duverger, A.; Berg, J.S.; Busigny, V.; Guyo, F.; Bernard, S.; Miot, J. Mechanisms of pyrite formation promoted by sulfate-reducing bacteria in pure culture. *Front. Earth Sci.* **2020**, *8*, 588310. [CrossRef]
100. Wacey, D.; Kilburn, M.R.; Saunders, M.; Cliff, J.; Brasier, M.D. Microfossils of sulphur-metabolizing cells in 3.4-billion-year-old rocks of Western Australia. *Nat. Geosci.* **2011**, *4*, 698–702. [CrossRef]
101. Duck, L.J.; Glikson, M.; Golding, S.D.; Webb, R.E. Microbial remains and other carbonaceous forms from the 3.24 Ga Sulphur Springs black smoker deposit, Western Australia. *Precambrian Res.* **2007**, *154*, 205–220. [CrossRef]
102. Schidlowski, M. Probable life-forms from the Precambrian of the Witwatersrand system (South Africa). *Nature* **1965**, *205*, 895–896. [CrossRef]
103. Guan, C.; Wang, W.; Zhou, C.; Muscente, A.D.; Wan, B.; Chen, X.; Yuan, X.; Chen, Z.; Ouyang, Q. Controls on fossil pyritization: Redox conditions, sedimentary organic matter content, and Chuaria preservation in the Ediacaran Lantian Biota. *Palaeo. Palaeo. Palaeo.* **2017**, *474*, 26–35. [CrossRef]
104. Lepot, K. Signatures of early microbial life from the Archean (4 to 2.5 Ga) eon. *Earth-Sci. Rev.* **2020**, *209*, 103296. [CrossRef]
105. Donald, R.; Southam, G. Low temperature anaerobic bacterial diagenesis of ferrous monosulfide to pyrite. *Geochim. Cosmochim. Acta* **1999**, *63*, 2019–2023. [CrossRef]
106. Bao, H.; Sun, T.; Kohl, I.; Peng, Y. Comment on "Early Archaean microorganisms preferred elemental sulfur, not sulfate". *Science* **2008**, *319*, 1336. [CrossRef] [PubMed]
107. Finster, K. Microbiological disproportionation of inorganic sulfur compounds. *J. Sulphur Chem.* **2008**, *29*, 281–292. [CrossRef]
108. Finster, K.; Liesack, W.; Thamdrup, B. Elemental sulfur and thiosulfate disproportionation by Desulfocapsa sulfoexigens sp. nov., a new anaerobic bacterium isolated from marine surface sediment. *Appl. Environ. Microbiol.* **1998**, *64*, 119–125. [CrossRef]
109. Holland, H.D. Systematics of isotopic composition of sulfur in oceans during the Phanerozoic and its implications for atmospheric oxygen. *Geochim. Cosmochim. Acta* **1973**, *37*, 2605–2616. [CrossRef]
110. Sugitani, K. Early Archean (Pre-3.0 Ga) Cellularly Preserved Microfossils and Microfossil-like Structures from the Pilbara Craton, Western Australia—A Review. In *Earth's Oldest Rocks*; van Kranendonk, M.J., Bennett, V.C., Hoffmann, J.E., Eds.; Elsevier: Amsterdam, The Netherlands, 2019; pp. 1007–1028. [CrossRef]
111. Wacey, D.; Noffke, N.; Saunders, M.; Guagliardo, P.; Pyle, D.M. Volcanogenic pseudo-fossils from the ~3.48 Ga Dresser Formation, Pilbara, Western Australia. *Astrobiology* **2018**, *18*, 539–555. [CrossRef]